DESIGN AND FABRICATION OF MICRO-CHANNELS AND NUMERICAL ANALYSIS OF DROPLET MOTION NEAR MICROFLUIDIC RETURN BENDS

A Thesis
Submitted to the Graduate Faculty
of the
North Dakota State University
of Agriculture and Applied Science

By

John-Luke Benjamin Singh

In Partial Fulfillment of the Requirements
for the Degree of
MASTER OF SCIENCE

Major Program:
Biomedical Engineering

April 2019

Fargo, North Dakota

North Dakota State University
Graduate School

Title

DESIGN AND FABRICATION OF MICRO-CHANNELS AND NUMERICAL ANALYSIS OF DROPLET MOTION NEAR MICROFLUIDIC RETURN BENDS

By

John-Luke Benjamin Singh

The Supervisory Committee certifies that this ***disquisition*** complies with North Dakota State University's regulations and meets the accepted standards for the degree of

MASTER OF SCIENCE

SUPERVISORY COMMITTEE:

Dr. Yechun Wang
Co-chair

Dr. Yan Zhang
Co-chair

Dr. Amanda Brooks

Dr. Mark Jensen

Approved:

26 April 2019
Date

Dr. Alan Kallmeyer
Department Co-chair

ABSTRACT

Three-dimensional spheroid arrays represent in vivo activity better than conventional 2D cell culturing. A high-throughput microfluidic chip may be capable of depositing cells into spheroid arrays, but it is difficult to regulate the path of individual cells for deposition. Droplets that encapsulate cells may aid in facilitating cell delivery and deposition in the return bend of a microfluidic chip. In this study, a low-cost method for fabricating polymer-cast microfluidic chips has been developed for rapid device prototyping. Computational fluid dynamic (CFD) simulations were conducted to quantify how a change in geometry or fluid properties affects the dynamics of a droplet. These simulations have shown that the deformation, velocity, and trajectory of a droplet are altered when varying the geometry and fluid properties of a multiphase microfluidic system. This quantitative data will be beneficial for the future design of a microfluidic chip for cell deposition into 3D spheroid arrays.

ACKNOWLEDGEMENTS

Without the guidance of Dr. Yechun Wang, this work would not exist. I extend my gratitude for her wisdom and kindness as a professor and a mentor. I am thankful for Dr. Yan Zhang who has challenged me to view difficult problems from every angle and come up with novel solutions. Dr. Amanda Brooks has shown immense generosity of her time and resources toward my projects. She has taught me to understand the value of true learning and cross-functional communication. Dr. Mark Jensen exhibits enthusiasm, patience, and intentionality as he supports students seeking to strengthen the bond between engineering and medicine.

I am grateful for the research assistance that was provided by Doug Mohr. I would like to thank my original project team of Ben Gerber, Kenzie Stark, and Kelsey Yon. The microfluidic chip fabrication process was developed based off advice from Dr. Dharmakeerthi Nawarathna. I would like to recognize my colleagues Ben Brooks, Dan Ewert, Julie Melbye, Chad Rehovsky, Joshua Liaw, Vidura Jayasooriya, Logeeshan Velmanicka, and Fleming Dackson for their interest and encouragement in my research.

My family has faithfully cared for me throughout my life. I am fortunate to know that I can always rely on my parents, Paul and Beth, and my siblings, John-Paul, John-Mark, Jaana, and Juliana. Thank you for encouraging me to strive for excellence in all that I do.

DEDICATION

To my intelligent and stunning fiancée, Ashley, who selflessly serves others from a compassionate heart. You strengthen my motivation and sharpen my character. Some seek after wealth and fame, but I have found greater worth in your companionship.

TABLE OF CONTENTS

LIST OF TABLES

LIST OF FIGURES

1. INTRODUCTION

A microfluidic chip is a device containing microchannels that is used to transport and manipulate small fluid volumes. Microfluidic chips offer a high throughput method for cell culturing and a rapid delivery of pharmaceutical drugs. Researchers working with microfluidic chips are often restricted in ordering new devices due to the cost and lead time of outsourced manufacturing. Advances in 3D printing technology enable the in-house fabrication of polymer cast microfluidic chips. The resolution of 3D printed polymer cast microfluidic chips cannot compete with conventional soft lithography practices, however, this low-cost alternative fabrication method is suitable for many applications. One research application involves forming droplets in multiphase flow. Droplets have gained popularity in pharmaceutical applications as a carrier to transport, protect, and release therapeutic molecules[1]. The motion of droplets formed by a T-junction in a channel can be optically analyzed under a microscopic camera. When altering channel geometry, it is more efficient to identify trends computationally than to fabricate a new microfluidic chip for each study. In this thesis, a model employing a 3D spectral boundary element method was used to study the effect of the capillary number, viscosity ratio, channel geometry, and gravity on the deformation, velocity, and trajectory of a droplet.

1.1. Various applications

Microfluidic chips are being applied to an increasing number of research areas due to their high-throughput platform, reduced fluid volume, and ability to manipulate the path of micron sized particles and cells. For example, microfluidic chips are being developed to analyze liquid biopsies by separating circulating tumor cells and identifying biomarkers[2]–[6]. Microfluidic chips are being used for 3D cell culturing which is a more accurate representation of the in vivo extracellular matrix than 2D cell culturing[7]. Microfluidic chips enable point-of-

care which allows for diagnostic testing at the bedside of the patient[8]. Using microfluidic chips for point-of-care diagnostics has the potential to improve patient outcomes because it is a less disruptive cell separation technique[9]. The concept of organ-on-a-chip provides the ability to imitate biological structures for disease interpretation and pharmaceutical drug testing[10]. Microfluidic droplet formation is suggested for testing antibiotics on bacteria and screening waterborne pathogens[11]. Within certain ranges, the device can consistently control the diameter of the droplet[12]. Only a few of the many applications of microfluidic chips have been listed regarding personalized medicine, liquid biopsies, drug testing, and droplet formation.

1.2. Fabrication techniques

An increase in microfluidic chip applications beckons for new fabrication techniques that reduce cost and improve the resolution of the devices. Microfluidic chips are made out of many materials including silicone, glass, ceramics, hydrogels, paper, elastomers, and other polymers[13]. Often polydimethylsiloxane (PDMS) is chosen as the chip material because it can bond with glass, has high optical transparency, forms well in molding, and is gas permeable[14]. Several techniques exist for fabricating microfluidic chips. The most common are wet or dry etching, thermoforming, direct writing with micro machines or lasers, and polymer casting with soft lithography[15]–[17]. Photolithography of SU8 photoresist is one of the most common methods for creating a master mold for PDMS chips. The resolution of modern 3D printers offers an alternative method for creating the master mold. 3D printing mitigates cost by eliminating the need for a clean room and speeds up the prototyping process, but this method is typically unable to achieve the resolution of lithography[18]. Recent research shows that shrinkage cycles could be used with 3D printed templates to isometrically reduce mold features and achieve a resolution as low as 4 μm[19]. This is accomplished by pouring a water-polyurethane mixture into a mold,

and after curing the polyurethane and evaporating the water, the features can isometrically shrink to half the original size.

1.3. Objectives of this work

The objectives of this work are to investigate how to manipulate the motion of a droplet moving through the return bend of a microfluidic chip. This study considers the effect that channel geometry, capillary number, viscosity ratio, and Bond number have on droplet deformation, velocity, and trajectory. A 3D spectral boundary element method is employed for the computational studies.

The polymer cast microfluidic chip fabrication process is presented in Chapter 2. The experimental droplet generation and optical analysis are presented in Chapter 3. The mathematical formulation behind the 3D spectral boundary element method is described in Chapter 4. The trends identified through the simulations are described in Chapter 5. A summary of the findings is presented in Chapter 6.

This is the first time that the 3D spectral boundary element method is applied to investigate the droplet dynamics of the particular geometry in a return bend. This work will support the design of microfluidic chips for cell deposition into 3D tumor spheroid arrays.

2. FABRICATION PROCESS

The microfluidic chips were fabricated using polymer casting of PDMS from a 3D printed master mold. This method was selected because it did not require any outsourced manufacturing and was successful in achieving a channel width of 150 μm which was suitable for the projected experiments. The fabrication process began with designing the master mold. SolidWorks 2014 computer aided design software was used to model the selected geometry. An example model of a master mold is shown in Figure 1.

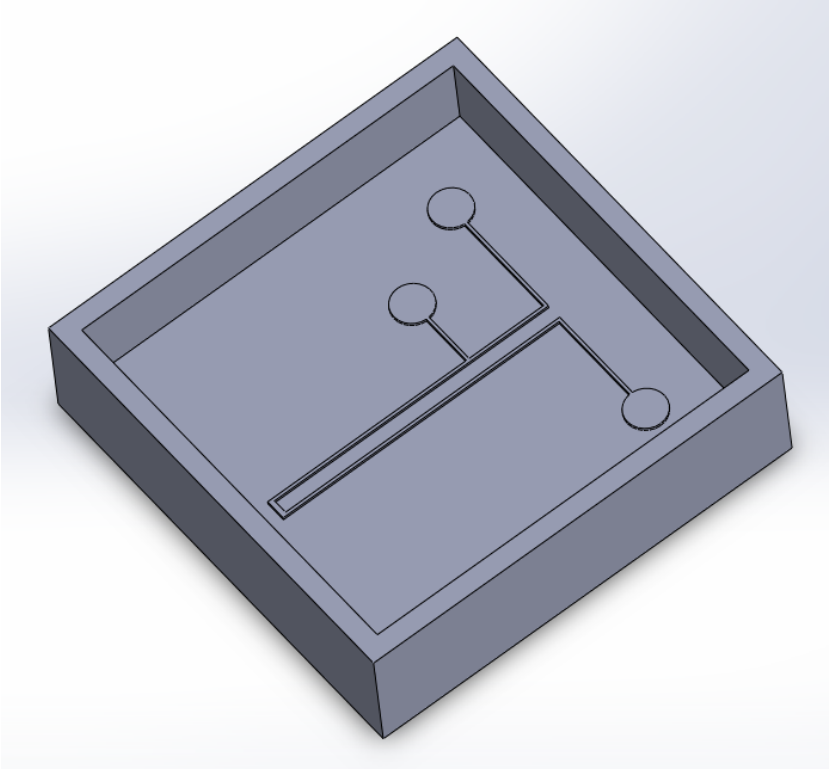

Figure 1. Model of master mold for microfluidic chip.

At the bottom of the mold in Figure 1, a return bend is shown where the channel turns 180°. This particular geometry was investigated because return bends are frequently utilized in microfluidic chips to conserve space and the bend could be modified to integrate a spheroid for the purpose of cell deposition. The design was exported as a .STL file and 3D printed with a clear resin on a Formlabs Form 2 stereolithography printer. The Form 2 was chosen because it

can create parts with a layer thickness as small as 25 microns. The photopolymer resin used was the Formlabs FLGPCL04 clear resin. Once the mold was printed, it was placed in an isopropyl alcohol bath. Stereolithography printers tend to leave uncured resin on the exterior surface of the finished part. The uncured resin was removed by rinsing the part in the isopropyl alcohol bath. The mold was allowed to cure for 12 hours under ultraviolent light.

The silicone chosen for the microfluidic chip was Dow Corning Sylgard 184. This was chosen because of the material transparency, a short cure time of 45 min at 100 °C, and a wide operational temperature range of -45 to 200 °C. Abiding by the manufacturer specifications, an uncured elastomer and curing agent were mixed at a 10:1 ratio in a conical centrifuge tube. After being stirred with a spatula for 3 minutes, the mixture was placed into a centrifuge to remove air bubbles. The centrifuge was set to run for 5 minutes at a speed of 2000 rpm and the temperature set to 4°C. Once removed from the centrifuge, the silicone mixture was poured into a fully cured 3D printed mold. The mixture was degassed in a vacuum chamber for 30 minutes. This degassing process removed air bubbles that were introduced to the silicone when it was poured into the mold. To speed up the silicone curing process, the surrounding temperature was increased by placing the mold in an incubator at 70 °C. After curing for 24 hours, the fully cured silicone was removed from the mold. A biopsy punch of 2 mm in diameter was used to create an inlet and outlet hole in the material.

The molding process produced three sides of the channel out of PDMS. A fourth wall was needed to close off the channel. Glass was selected because of its high transparency and ability to bond with silicone. The PDMS chip was bonded to a glass slide using oxygen plasma bonding. In oxygen plasma bonding, oxygen gas is flowed into a chamber and electrical currents are used to treat surfaces with plasma. This increases the surface energy of the material which

also increases its adhesion potential. A Trion RIE Plasma Etcher was used for the oxygen plasma bonding process. The machine was set at a power level of 100 W, a pressure level of 200 mTorr, a process time of 20 s, and an oxygen gas rate of 100 ccm. After treating the surface of the PDMS and the glass with plasma, the two materials were pressed together. To promote a strong bond the device was placed in an oven at 80°C to cure for one day. After curing, functional testing was performed by flowing water through the device and inspecting the seal for leaks. A fabricated microfluidic chip is shown in Figure 2.

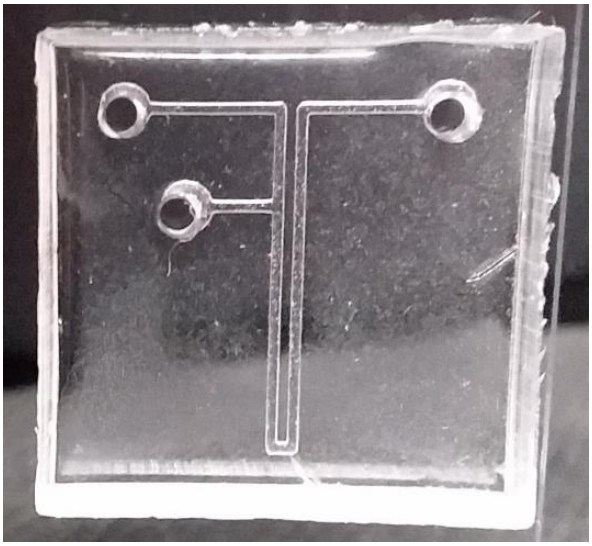

Figure 2. Polymer cast microfluidic chip bonded to glass.

2.1. Microscopic particle image velocimetry

Microscopic particle image velocimetry (micro-PIV) is an optical flow measurement method which couples the epi-florescent microscope and the traditional PIV setup. The optical method utilizes seeding particles that emit florescence when excited by a laser. A double pulse laser is synchronized with a charge-coupled device camera. The camera captures a pair of images of the fluorescent particles over a short time interval. Cross-correlation analysis is then conducted to calculate the particle displacement over the time interval to generate a velocity field of the particles in the flow. The experimental setup for this method is shown in Figure 3.

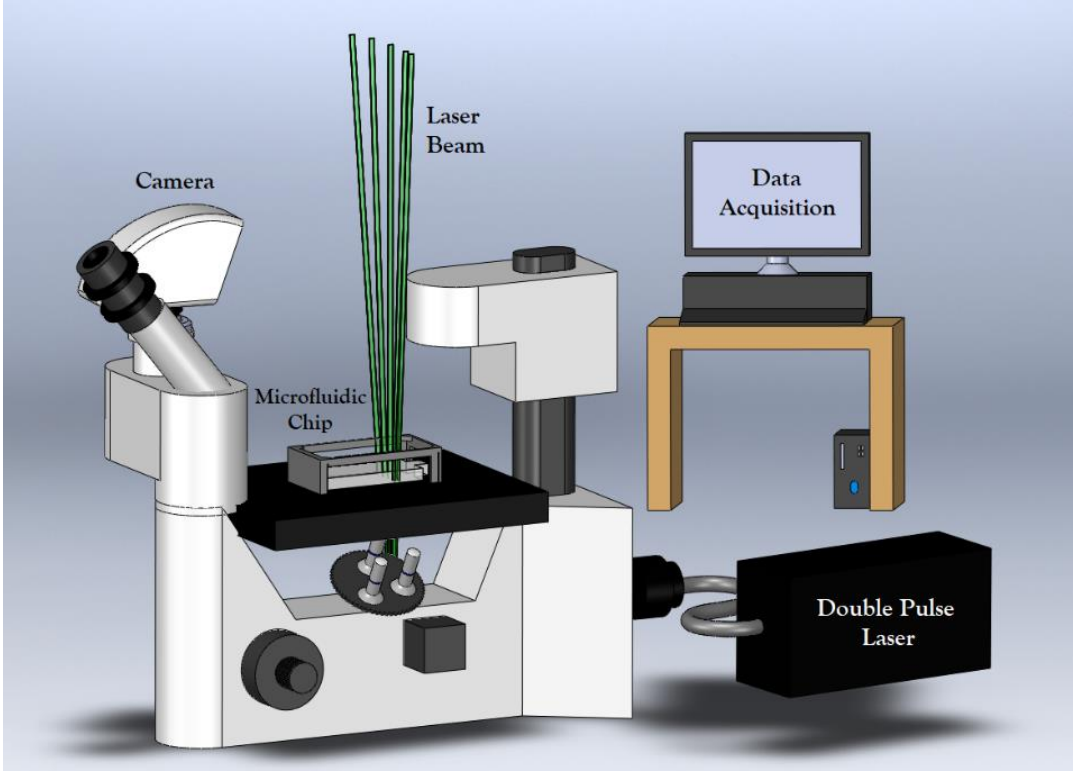

Figure 3. Microscopic particle image velocimetry experimental setup

In this study, the fluid flow around the return bend was analyzed using micro-PIV. Rhodamine B-marked particles of 1 μm that had an excitation wavelength of 540 nm and an emission wavelength of 584 nm were chosen. In this frequency range, the particles would emit florescence when placed in the volumetric illumination of a green (532 nm) laser. The volumetric flow rate was driven by a syringe pump at a rate of 0.1 mL/min. This produced a Reynolds number = 1. The Reynolds number (Re) is a dimensionless number that shows the ratio of the inertial forces over the viscous forces. The Reynolds number is useful for determining the flow regime. The flow is laminar when Re < 2300, transitional flow occurs when Re is between 2300 and 4000, and turbulent flow occurs when Re > 4000. Microfluidic chips typically deal with laminar flow conditions due to the small channel dimensions. Figure 4 shows the vertical velocity contour and velocity profiles at selected cross-sections of the microfluidic channel. The maximum velocity of the fluid was calculated as 0.025815 m/s.

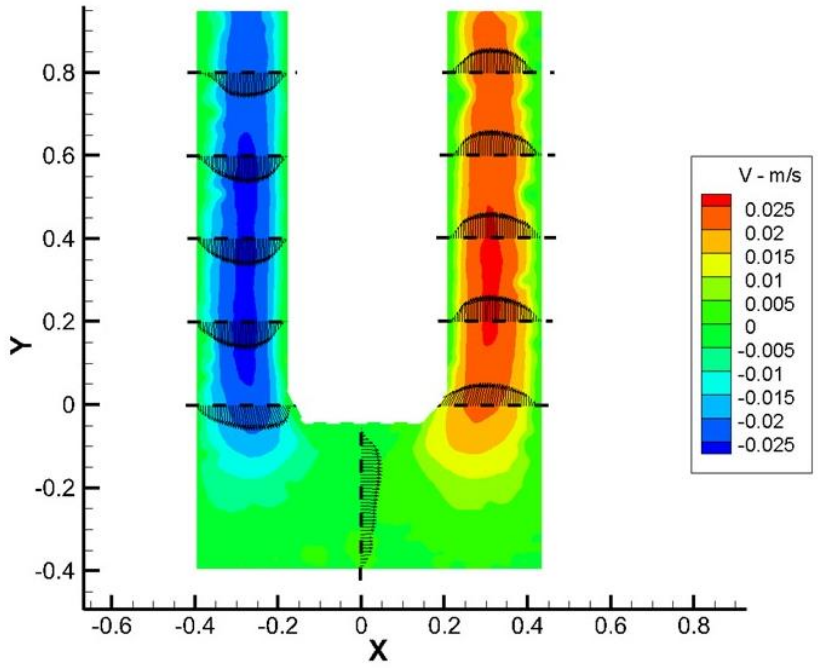

Figure 4. Vertical velocity contour and velocity profiles at selected cross-sections of the microfluidic channel return bend.

2.2. Design verification

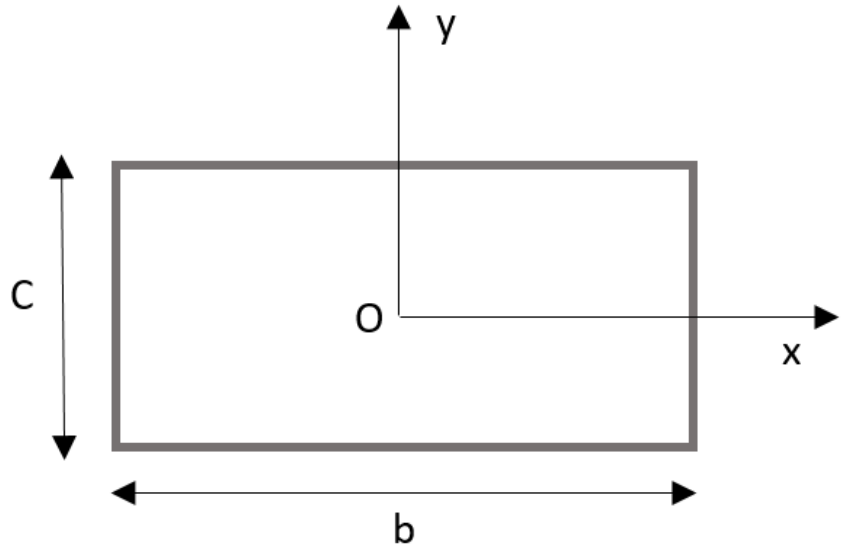

Figure 5. Rectangular channel coordinate system

Due to the buildup of process error in manufacturing, it is necessary to verify final product dimensions. A syringe needle was selected as a reference object and measured with a micrometer. The syringe needle and microfluidic channel were placed in the frame of the microscopic camera and an image was captured. The known diameter of the syringe needle was compared to the number of pixels in the image. With a distance assigned to each pixel, the channel width was able to be calculated. Due to a lack of transparency in the side view, the depth of the channel was unable to be measured optically. This measurement could be taken using a destructive method such as slicing the device open and using direct measurement, but a method of indirect measurement of the channel depth also exists. It requires the maximum velocity of the fluid from the micro-PIV experiment and the volumetric flow rate from the syringe pump. With this information, the channel depth was able to be determined using the following method. For a coordinate system as defined by Figure 5 the velocity can be expressed by Equation 1 for steady unidirectional flow in a channel.

$$Uz = \frac{1}{2u}(K + \rho g \sin\beta)\left(\frac{c^2}{4} - y^2\right) + \sum_{n=1}^{\infty} A_n cosh\frac{2\alpha_n x}{c} cos\frac{2\alpha_n y}{c} \quad (1)$$

where $A_n = (-1)^n \frac{c^2}{2\mu\alpha_n^3}\frac{(K+\rho g\, sin\beta)}{\cosh(\alpha_n\, b/c)}$ and $\alpha_n = \frac{(2n-1)\pi}{2}$, μ is the viscosity of the fluid, β is the inclination angle between the horizontal plane and channel axis direction, and $K = -\frac{\partial P}{\partial z}$ is the pressure gradient [20].

Recognizing that the maximum velocity occurs at coordinate (0,0) in the channel, a relationship can be obtained for the maximum velocity by substituting x=0 and y=0 into the U_z velocity equation. A flow rate calculation can be done by integrating the flow velocity equation over the width and depth, b and c, of the channel.

$$Q = \iint_{-\frac{b}{2}-\frac{c}{2}}^{\frac{b}{2}\frac{c}{2}} U\, dy\, dx \quad (2)$$

Although the pressure gradient is unknown, by dividing the flow rate by the maximum velocity, the pressure gradient term drops out. An equation with one unknown, the channel depth c, is established. By employing the bisection method, the depth of the channel was calculated as 45.8 μm. This value was much smaller than the expected depth of 150 μm. The dimensional difference could be explained in part by too much pressure causing the PDMS to deform during the oxygen plasma bonding process. This reveals one of the imperfections of the fabrication process. Currently, dimensional consistency is not able to be achieved when creating the microfluidic chips. This is primarily attributed to a lack of precision in the Formlabs Form 2 3D printer and the silicone deforming during the oxygen plasma bonding process. Although the final product is inconsistent with the dimensions of the original design, the microfluidic chips are still valuable for experiments because the function of the device is not compromised, and the dimensions can be measured or calculated. Additionally, through attempting to verify the channel dimensions, a valuable method for calculating the channel depth based of the channel width and maximum fluid velocity was developed.

3. DROPLET FORMATION AND OPTICAL ANALYSIS

An experiment was conducted to optically measure the dynamics of a droplet moving through the previously fabricated microfluidic chip. The microfluidic chip was designed with a T-junction for droplet formation. A Prosilica GC microscope was used to capture images at a frame rate of 30 frames per second. Canola oil was used for the continuous phase with a viscosity of 0.890 cP at 25°C and a density of 997 kg/m^3. Water was used for the discontinuous phase with a viscosity of 54 cP at 25°C and a density of 914 kg/m^3. A Chemyx Fusion 4000 syringe pump was selected to drive the volumetric flow rate of the continuous phase at 0.19 mL/hr and the discontinuous phase at 0.0019 mL/hr. The interfacial surface tension between the two fluids was 26.2 mN/m and the capillary number was calculated as 6.08x10^{-4}. Images of the droplet at 1.5x magnification for different locations in the microfluidic chip are shown by Figure 6.

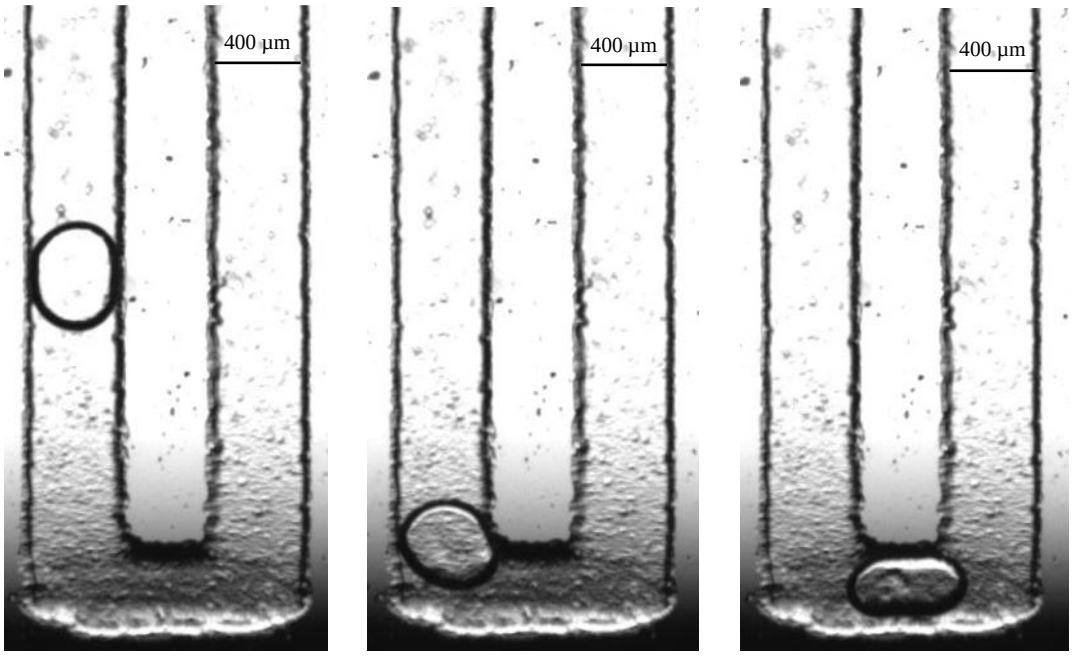

(a) (b) (c)

Figure 6. Droplet moving through (a) straight channel (b) corner of bend (c) middle of return bend.

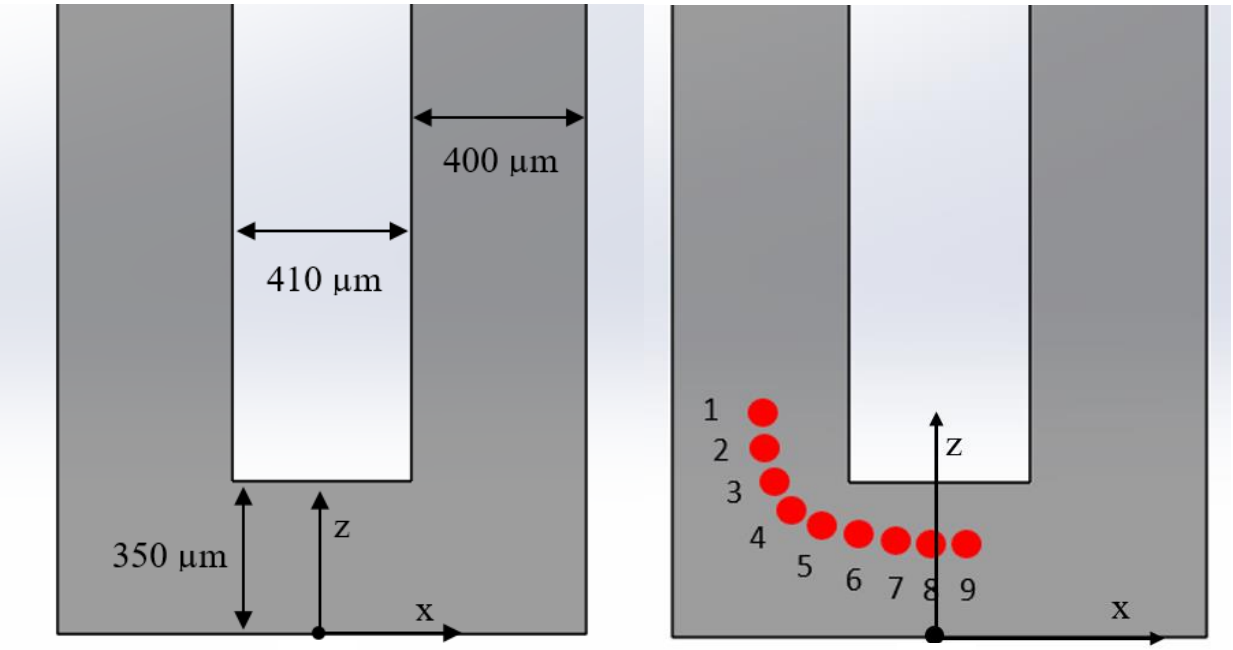

Figure 7. Optically measured return bend channel dimensions (a) and data point reference in the x-z plane (b).

Using a syringe needle as a reference object, the actual channel dimensions in the x-z plane were calculated from the image pixels as shown by Figure 7a.

It is recognized that the image based measurements taken by hand are subject to human error. However, the purpose of this study was to test the functionality of the microfluidic chip and provide proof of concept for the future development of image processing software for the analysis of droplet dynamics in a microchannel.

The velocity, *Uz*, of the droplet leading interface was calculated in the straight section of the channel. This calculation was performed for 11 droplet images with the average droplet velocity calculated as 1.028 mm/s with a standard deviate of 0.044 mm/s.

For the return bend region of the channel, the U_z and U_x velocity was calculated for the droplet centroid. The velocities are plotted as a function of the centroid location z_c to act as a position guide for the droplet moving through the channel. Nine data points of the droplet

moving from the inlet channel toward the return bend were calculated based off the optical measurements as shown in Figure 7b. The location z_c=0 is considered as the center of the return bend.

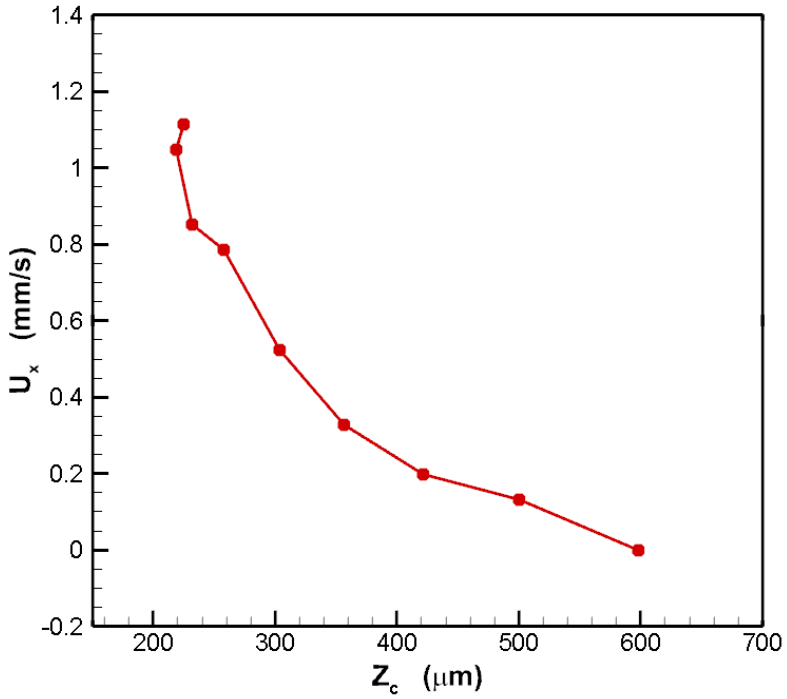

Figure 8. Centroid velocity U_x plotted as a function of the centroid location z_c.

Figure 8 shows the centroid velocity U_x plotted as a function of the centroid location z_c. It is noted that as the droplet moves toward the center of the return bend, the velocity U_x increases. This is explained by the 90° bend in the channel changing the direction of the flow.

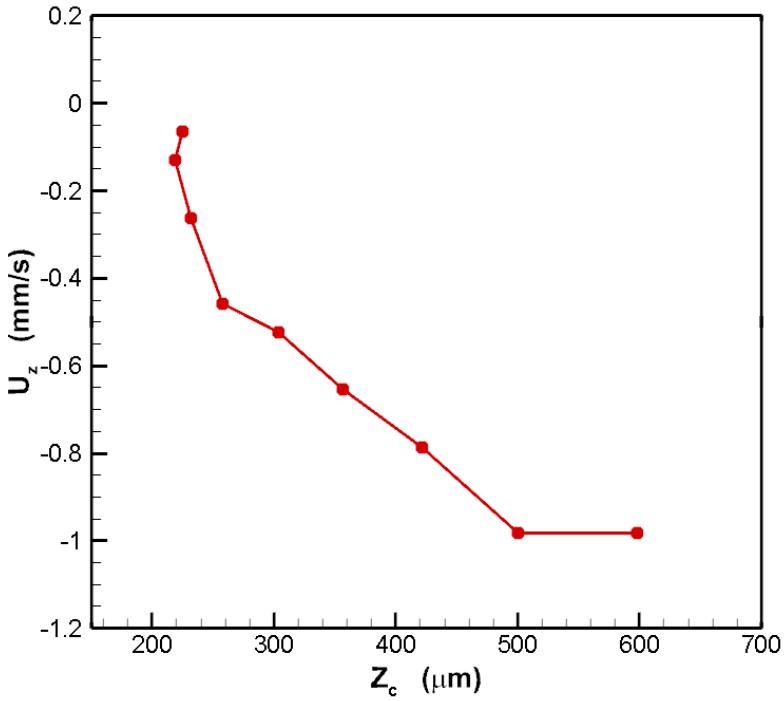

Figure 9. Centroid velocity U_z plotted as a function of the centroid location z_c.

Figure 9 shows the centroid velocity U_z plotted as a function of centroid location z_c. It is seen that the velocity U_z is initially large, but as the droplet moves toward the center of the return bend, the velocity continually decreases. Next, the droplet deformation was calculated. The droplet deformation was defined as

$$D = \frac{l_z - l_x}{l_z + l_x} \tag{3}$$

where l_z is the length corresponding to the longest axis of the droplet and l_x is the length corresponding to the shortest axis of the droplet. Figure 10 shows the droplet deformation D plotted as a function of centroid location z_c.

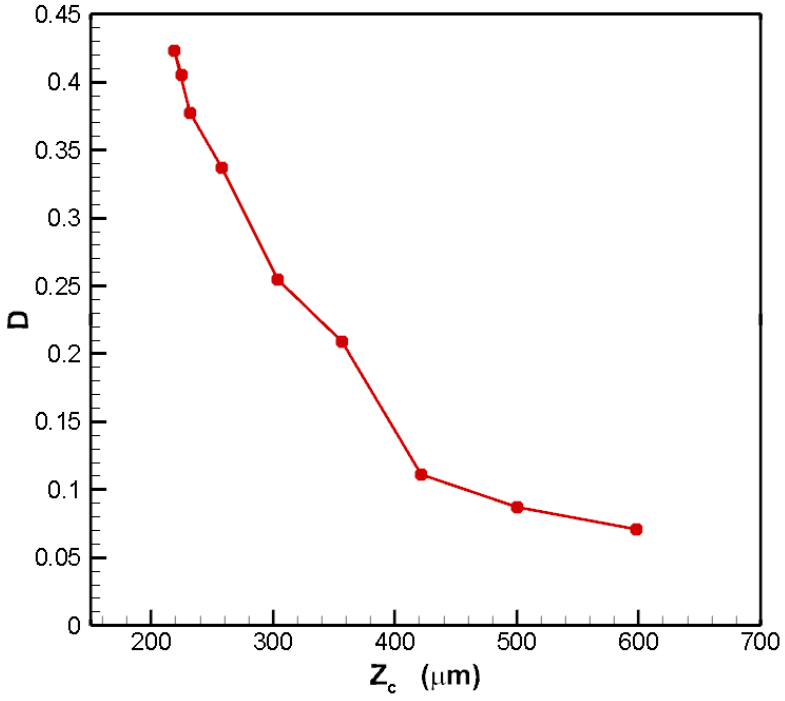

Figure 10. Droplet deformation D plotted as a function of centroid location z_c.

In Figure 10 the droplet deformation is initially low but increases as the droplet moves toward the center of the return bend. This agrees with the velocity, U_x, being largest near the center of the return bend because a droplet that is deformed into the shape of a bullet will have less resistance as it moves through the suspending fluid.

3.1. Limitations of the experiment

One limitation of the experiment is the large surface roughness of the channel walls. As the width of the channel is decreased, the relative roughness of the channel walls increases. This is due to the 25 μm resolution of the 3D printer used for the fabrication of the molds. However, smoother channel walls could be obtained with better 3D printing technology. Another limitation is the inability to manufacture perfect 90° bends in the channel. This is a result of the cured elastomer deforming when being removed from the mold. For this experiment, the channel depth was not measured and the calculations were performed under the assumption that the channel

was perfectly square. In reality, the channel depth is expected to be a value less than the channel width. The channel depth could be calculated using the method described in section 2.2 by first inserting particles in the flow that followed the fluid streamlines to calculate the maximum fluid velocity.

The results from this study prove the functionality of the microfluidic chip through the formation of droplets in multiphase flow. The manual, optical analysis recognized trends of velocity and deformation of the droplet moving through the return bend. Future work should use image analysis software to increase the accuracy of the data measurements.

4. MATHEMATICAL FORMULATION

In this chapter dimensionless numbers are discussed, the geometry is defined for the microfluidic chip that was studied, the mathematical formulation behind the computation model is presented, and the model is validated.

4.1. Dimensionless numbers

When dealing with microsystems, it can be difficult to identify what forces are influencing particle movement. Dimensionless numbers alleviate this difficulty by presenting the relationship between different forces. This section introduces three dimensionless numbers that were significant for the computational analysis of a droplet moving through a return bend. The Reynolds number, as previously mentioned, is a calculation of the inertial forces over the viscous forces. The equation for the Reynolds number is

$$Re = \frac{\boldsymbol{\rho u L}}{\mu} \tag{4}$$

where ρ is the fluid density, $\boldsymbol{u}$ is the velocity, μ is the dynamic viscosity, and L is the characteristic length. The Reynolds number (Re) establishes whether the flow regime is laminar, transitional, or turbulent.

The Bond number (Bo) compares the effect over gravitational forces over surface tension forces. The equation for the Bond number is

$$Bo = \frac{\Delta \rho g L^2}{\sigma} \tag{5}$$

where Δρ is the difference in density between the two phases, g is the gravitational acceleration, L is the characteristic length, and σ is the surface tension.

The capillary number (Ca) calculates the relationship of the viscous forces over the surface tension forces. The equation for the capillary number is

$$Ca = \frac{\mu \boldsymbol{u}}{\sigma} \tag{6}$$

where μ is the dynamic viscosity, $\boldsymbol{u}$ is the velocity, and σ is the surface tension.

4.2. Governing equations and boundary conditions

The return bend geometry of the microfluidic chip is shown in Figure 11 11.

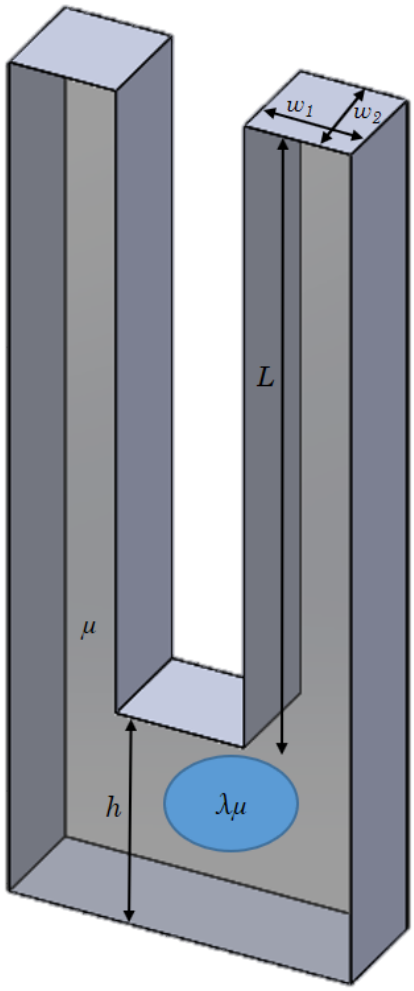

Figure 11. The geometry of a return bend in a microfluidic chip.

The mathematical formulation begins by establishing the governing equations for a droplet moving through the return bend in a microchannel. Due to a low reynolds number, the inertial terms are neglected in the Navier-Stokes equation. This simplifies the equation to the Stokes equation

$$\nabla \cdot \boldsymbol{\sigma} = -\nabla p + c\nabla^2 \boldsymbol{u} = 0 \tag{7}$$

The other governing equation is the Continuity equation

$$\nabla \cdot \boldsymbol{u} = 0 \tag{8}$$

where $\boldsymbol{\sigma}$ is the stress tensor, p is the dynamic pressure, c is the viscosity of the fluid such that c=μ for the suspending fluid and c=λμ for the droplet, and $\boldsymbol{u}$ is the velocity vector. The size of the droplet is provided by the equation

$$a = \left(\frac{3V}{4\pi}\right)^{1/3} \tag{9}$$

where V is the droplet volume. The density of the two fluids is chosen to be equal, $\rho_1 = \rho_2$, and it is assumed that the surface tension is constant across the surface of the droplet. The droplet deformation is defined the same way that it was in Equation 3.

Examining the boundary conditions on the bridge interface, it is noted that

$$\boldsymbol{u} = \boldsymbol{u}_i = \boldsymbol{u}_o \tag{10}$$

$$\Delta \boldsymbol{f} \equiv \boldsymbol{f}_o - \boldsymbol{f}_i = \frac{\mu U}{Ca}(\nabla s \cdot \boldsymbol{n})\boldsymbol{n} \tag{11}$$

where the subscripts "i" and "o" represent the droplet and the suspending fluid respectively and ∇s is the gradient of the droplet interface. The normal direction, $\boldsymbol{n}$, is into the continuous phase. The other system boundary conditions are

$$u = 0 \; at \; wall \; surface \; S^w \tag{12}$$

$$u = u^\infty \; at \; fluid \; interface \; S^f \tag{13}$$

The steady unidirectional flow in the rectangular channel far from the droplet and the return bend is given by[20]

$$u_z^\infty / B = w_2^2 - y^2 + \sum_{n=1}^{\infty} A_n \, cosh\left(\alpha_n \frac{x}{w_2}\right) cos(\alpha_n \frac{y}{w_2}) \tag{14}$$

where

$$B = -\frac{\partial p/\partial z}{2\mu} \tag{15}$$

$$A_n cosh(\alpha_n w_1/w_2) = (-1)^n 4 w_2^2 B/\alpha_n^3 \tag{16}$$

$$\alpha_n = (2n-1)\pi/2 \tag{17}$$

The variables w_1 and w_2 are in reference to the channel dimensions of the rectangular cross section. Eqns. (15) – (18) define the origin of the coordinate system to be in the center of the rectangular cross section. The average velocity of the flow far from the droplet and the return bend may be derived as

$$U/B = \frac{2}{3}w_2^2 + \sum_{n=1}^{\infty}(-1)^n \frac{w_2^3}{w_1}\frac{4}{\alpha_n^5} sin(\alpha_n)\, tanh(\alpha_n w_1/w_2) \tag{18}$$

In Eqn. 5 and Eqn. 9, because terms with n $\geq$ 50 are neglected in our computations, a truncation error of O(10^{-9}) exists.

4.3. Boundary integral equation

The governing equations of the Stokes equation and the Continuity equation are used to develop the boundary integral equation (BIE)[21]. The velocity for an arbitrary point $\mathbf{x}_o$ on the droplet interface Γ, solid wall boundary S_w, and fluid boundaries S_f, satisfy the following boundary integral equation

$$\Omega \boldsymbol{u}(\boldsymbol{x}_o) =$$

$$-\int_{\Gamma}[\boldsymbol{S}\cdot\Delta\boldsymbol{f} - \mu(1-\lambda)\boldsymbol{T}\cdot\boldsymbol{u}\cdot\boldsymbol{n}]\,dS$$

$$-\int_{S_w}[\boldsymbol{S}\cdot\boldsymbol{f_2} - \mu\boldsymbol{T}\cdot\boldsymbol{u_2}\cdot\boldsymbol{n}]\,dS$$

$$-\int_{S_f}[\boldsymbol{S}\cdot\boldsymbol{f_2} - \mu\boldsymbol{T}\cdot\boldsymbol{u_2}\cdot\boldsymbol{n}]\,dS \tag{19}$$

where $\Omega = 4\pi\mu(1+\lambda)$ for an arbitrary point, $\mathbf{x}_o$, on the droplet interface, microfluidic wall, and the other boundaries. **S** is the fundamental solution for the velocity from the Stokes equation and **T** is the corresponding stress[22], [23]. A detailed derivation is provided in Pozrikidis[24].

The boundaries of the channel, fluid, and droplet interface are discretized into a moderate number N_E of surface elements. The surface elements are mapped by parametric variables ξ and

η on a square interval [-1,1][25]. The time integration uses an explicit Runge-Kutta method[26]. The 3D spectral boundary element discretization of the droplet and the return bend are shown in Figure 12.

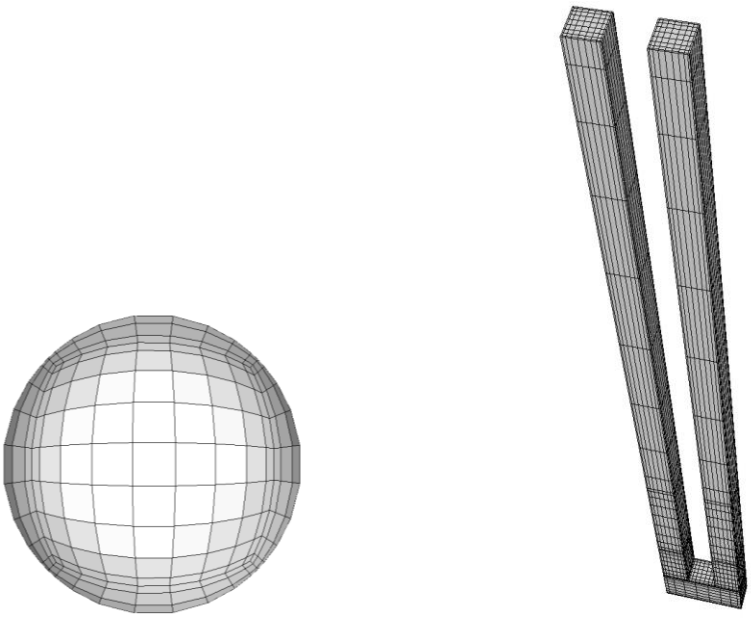

(a) (b)

Figure 12. 3D spectral boundary element discretization of droplet (a) and return bend (b).

4.4. Validation

For computational studies, convergence tests should be conducted to ensure the accuracy of results while minimizing computational cost. A convergence test was performed to validate the accuracy of the numerical solution as shown by Figure 13.

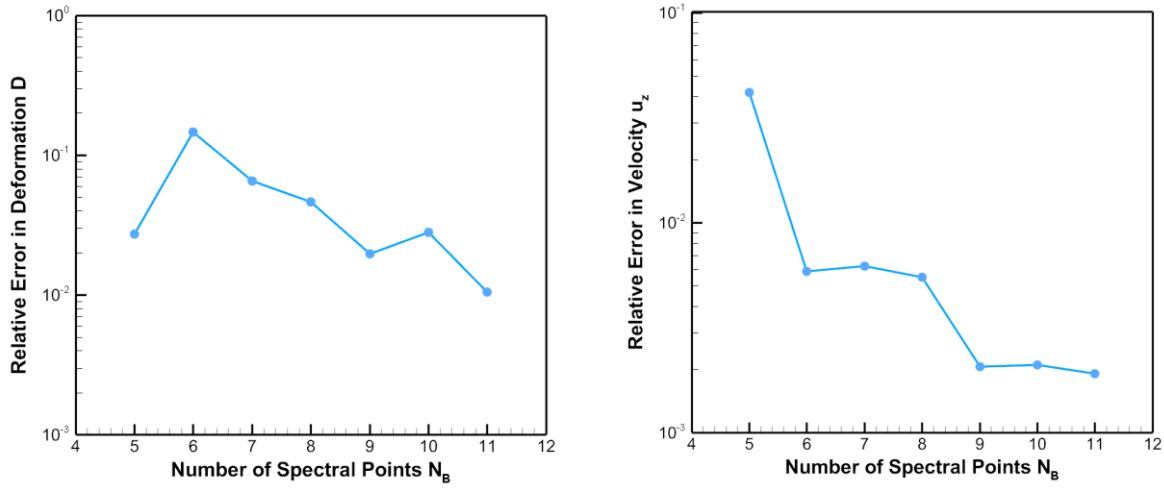

(a) (b)

Figure 13. Absolute relative error in (a) deformation D and (b) velocity U_z at time t = 1 for NB =5, 6, 7, 8, 9, 10, 11. The values for NB = 12 are used as the base in calculating the relative error. The computations are carried out for Ca = 0.05, λ = 0.2, h2 = 3.33. And the droplet size a = 0.8.

From the convergence study, it can be seen that 11 spectral points should be used to reduce the relative error for computing deformation. However, for velocity, the relative error was minimal with only 9 spectral points. For the computational studies in this thesis, 11 spectral boundary points were used.

5. COMPUTATIONAL RESULTS AND DISCUSSION

In the computational studies, lengths are non-dimensionalized with the channel width w, velocities with the average channel velocity *U*, and times with $\tau_f = w/U$. The deformation, velocity, and trajectory of a droplet moving through a return bend were investigated under various conditions of channel geometry, fluid properties, and the influence of gravity. It is valuable to have the initial height of the droplet be lower in the channel to reduce the computation cost of the simulation. The initial height of the droplet centroid was defined as 5 times the channel width. To validate that this was far enough away from the return bend, a study was conducted where the droplet centroid started at a height of 5, 10, and 15 times channel width. For this study, *Ca* = 0.03, *Bo* = 0, λ = 0.2, and *h* = 2. The following figures compare the droplet deformation, velocity U_x and U_z, and the centroid trajectory for each case.

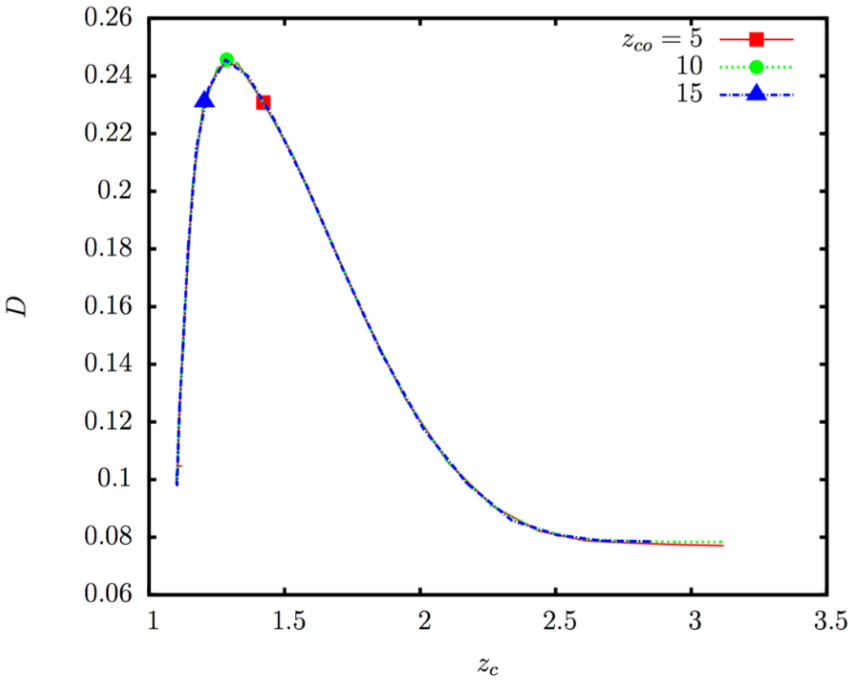

Figure 14. Droplet deformation D is plotted as a function of its centroid location z_c. Cases for z_{c0} = 5, 10, and 15 are included.

All three cases follow the same trend of increasing in deformation as the droplet moves around the corner of the return bend and decreasing in deformation very close to the middle of the return bend.

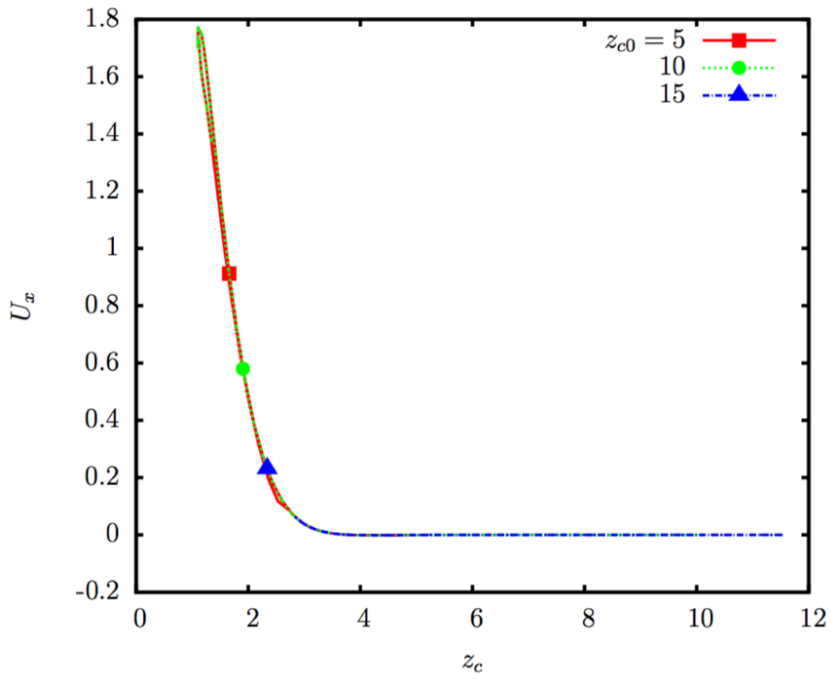

Figure 15. Droplet velocity U_x is plotted as a function of its centroid location z_c. Cases for z_{c0} = 5, 10, and 15 are included.

All three cases show the trend of the initial velocity, U_x, being very close to zero and increasing to a maximum value near the center of the return bend.

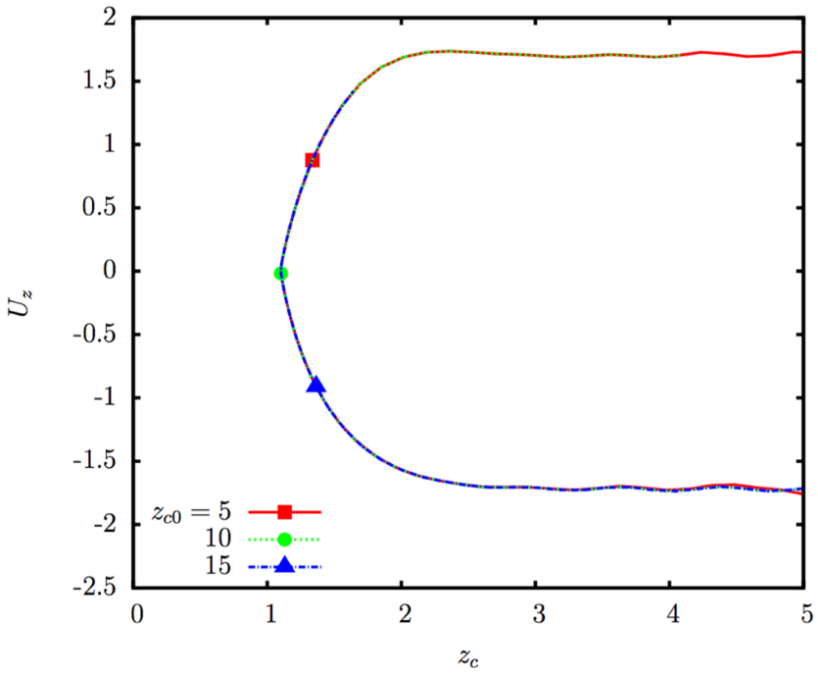

Figure 16. Droplet velocity U_z is plotted as a function of its centroid location z_c. Cases for z_{c0} = 5, 10, and 15 are included.

All three cases show the same trend of the velocity U_z being greatest in the inlet and outlet channels and reaching a value of zero near the middle of the return bend.

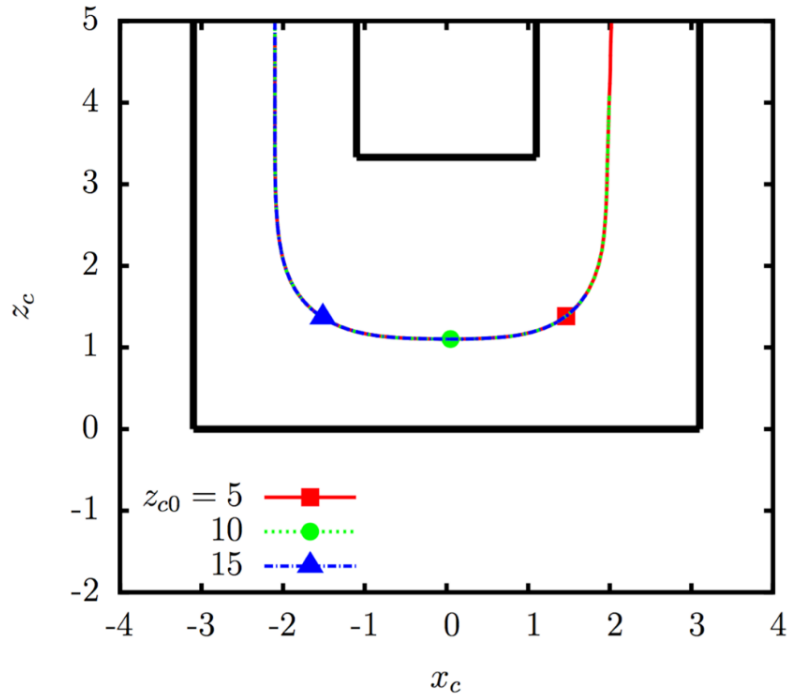

Figure 17. Trajectory of the droplet centroid. Cases for z_{c0} = 5, 10, and 15 are included.

Figure 17 shows the droplet following the same trajectory for the three cases. For all the studies, is noted that the deformation, droplet velocity, and trajectory visually appear nearly identical for each droplet starting height. The case of $z_{c0} = 15$ was only computed to the second bend due to the high number of iterations. Table 1 compares the actual deformation for each droplet when $z_c = 1.2$.

Table 1. Percent difference calculation of deformation for $z_{co} = 5$, 10, and 15.

Time	Deformation	%Difference
2.49	0.2293	N/A
5.39	0.2294	0.0146
8.23	0.2295	0.0796

Table 1 shows that the deformation in the droplets starting at different heights is less than 1% different. This supports using $z_{co} = 5$ for the initial droplet height in the channel which reduces the computational time compared to starting the droplet at a higher location in the channel.

5.1. Influence of capillary number

The capillary number has been studied to recognize the effect that surface tension forces have on deformation, velocity and trajectory. Cases of $Ca = 0.01$, 0.03, and 0.05 have been considered. For this study, $z_{c0} = 5$, $Bo = 0$, $\lambda = 0.2$, and $h = 3.33$.

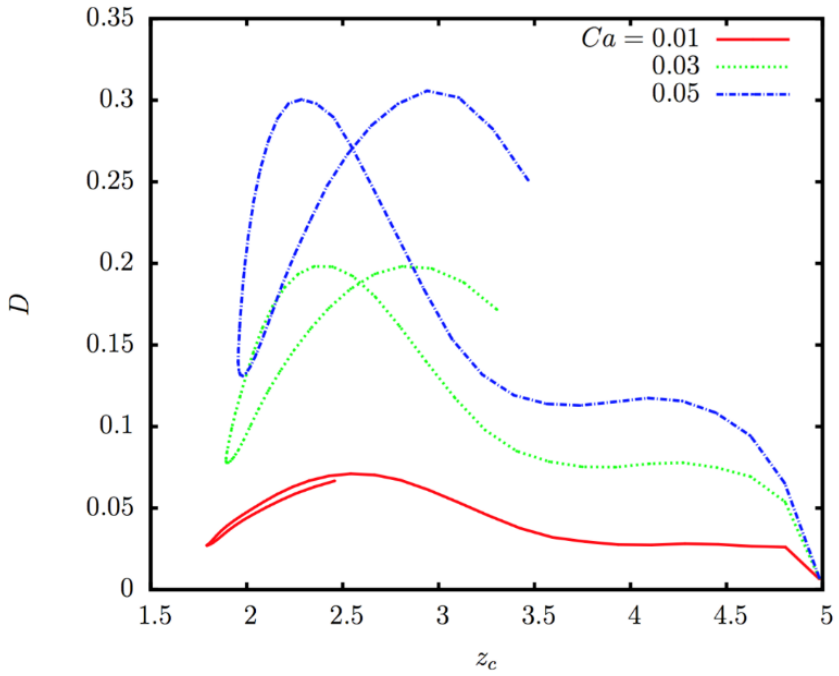

Figure 18. Droplet deformation D is plotted as a function of its centroid location z_c. Cases for Ca = 0.01, 0.03, and 0.05 are included.

When the droplet is moving through the inlet channel, the deformation is moderate. However, as the droplet moves around the corner, the deformation increases. The droplet relaxes as it moves through the middle of the return bend, but increases to a high level of deformation as it moves through the second corner toward the outlet channel.

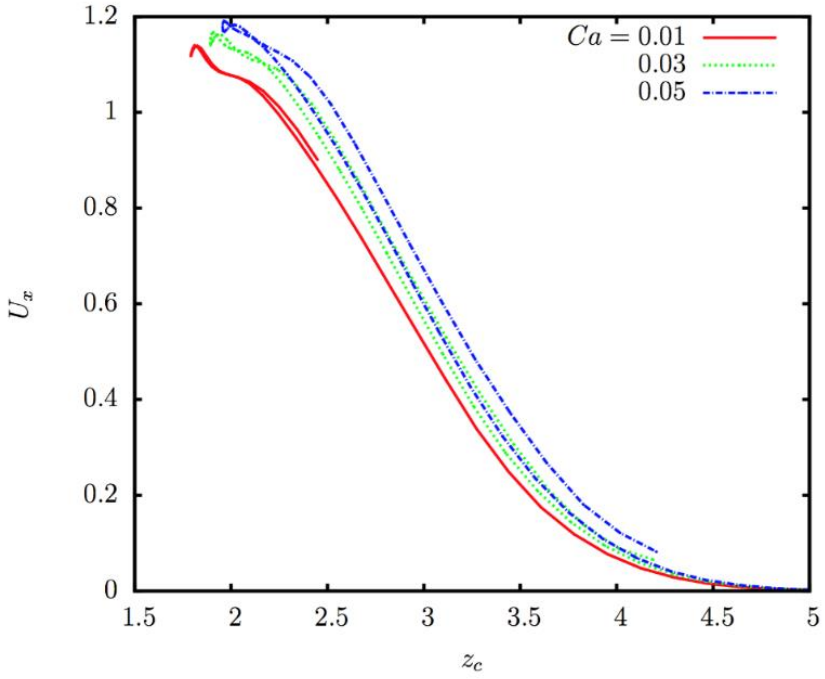

Figure 19. Droplet velocity U_x is plotted as a function of its centroid location z_c. Cases for Ca = 0.01, 0.03, and 0.05 are included.

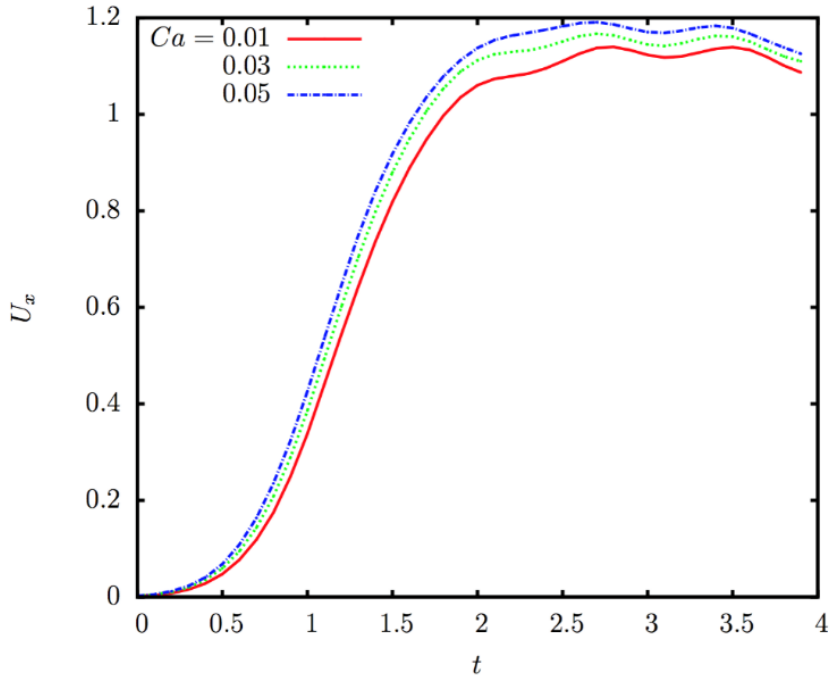

Figure 20. Droplet velocity U_x is plotted as a function of time. Cases for Ca = 0.01, 0.03, and 0.05 are included.

In Figure 19 and 20 the droplet velocity U_x increases until it begins to surpass the average flow rate of the continuous phase. When this occurs, the droplet velocity levels off until the droplet begins to slow down as it moves around the second corner toward the outlet channel.

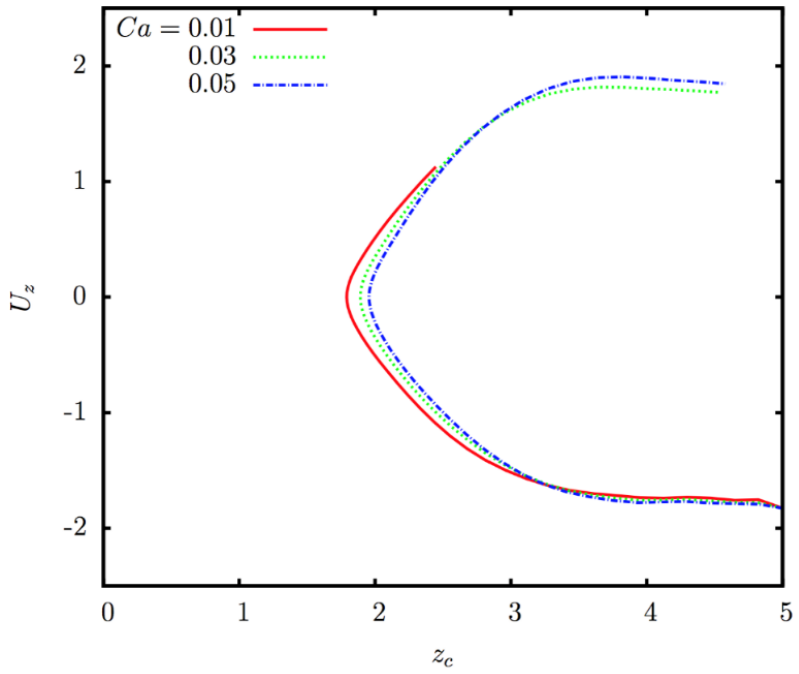

Figure 21. Droplet velocity U_z is plotted as a function of its centroid location z_c. Cases for Ca = 0.01, 0.03, and 0.05 are included.

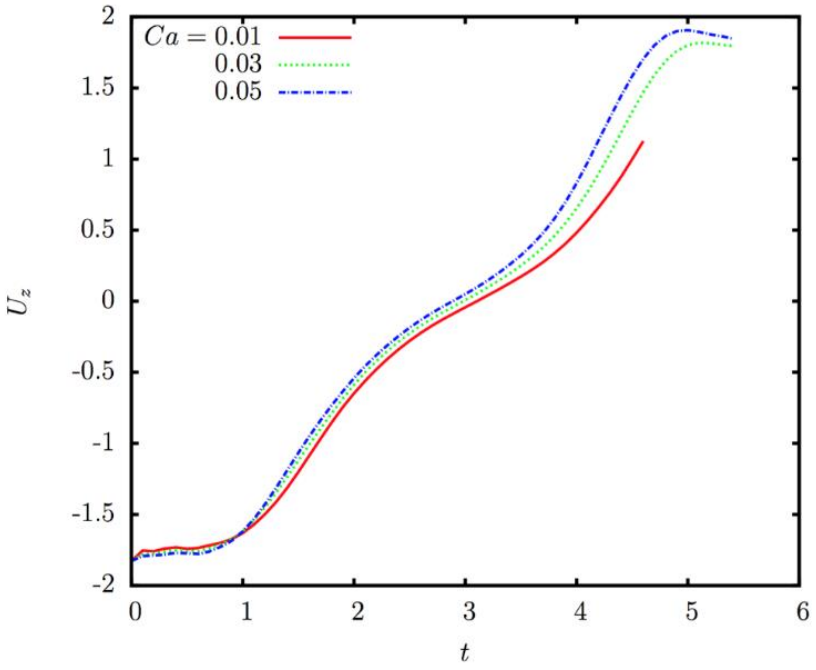

Figure 22. Droplet velocity U_z is plotted as a function of time. Cases for Ca = 0.01, 0.03, and 0.05 are included.

Figure 21 and 22 show that the droplet velocity U_z is largest in the inlet and outlet channel. As the droplet moves through the return bend, the velocity slows down until it eventually reaches zero in the center of the bend. At that point the velocity begins to increase as the droplet moves toward the outlet channel.

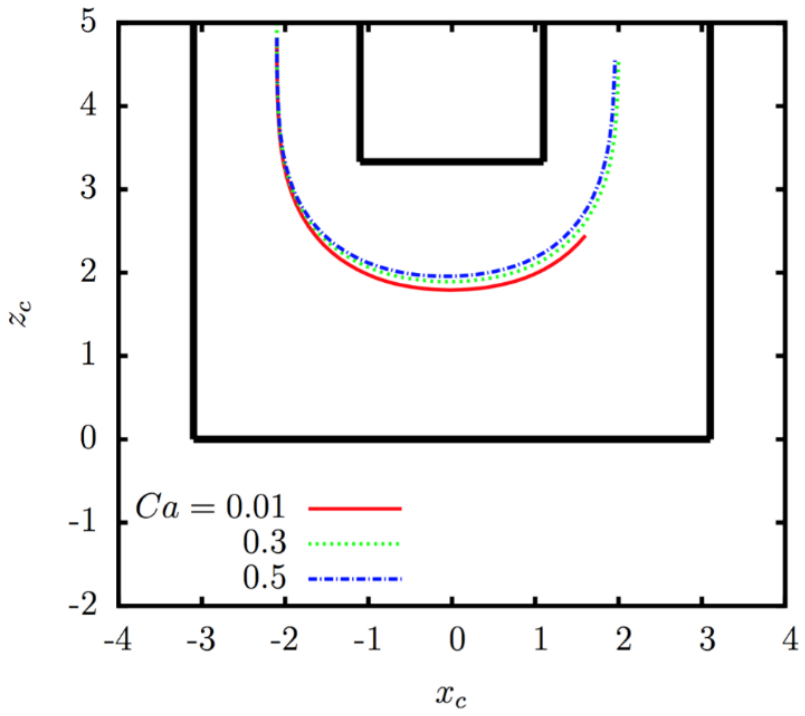

Figure 23. Trajectory of the droplet centroid. Cases for Ca = 0.01, 0.03, and 0.05 are included.

The previous figures show the trends that as the Ca number increases, the droplet deformation increases, the U_x and U_z velocities increase, and the trajectory of the droplet is higher as it moves through the return bend. With an increase in the Ca number, the surface tension forces decrease in relation to the viscous forces. The viscous forces retarding the droplet molecules cause the dispersed phase to deform into a bullet shape. This phenomenon is shown in Figure 24.

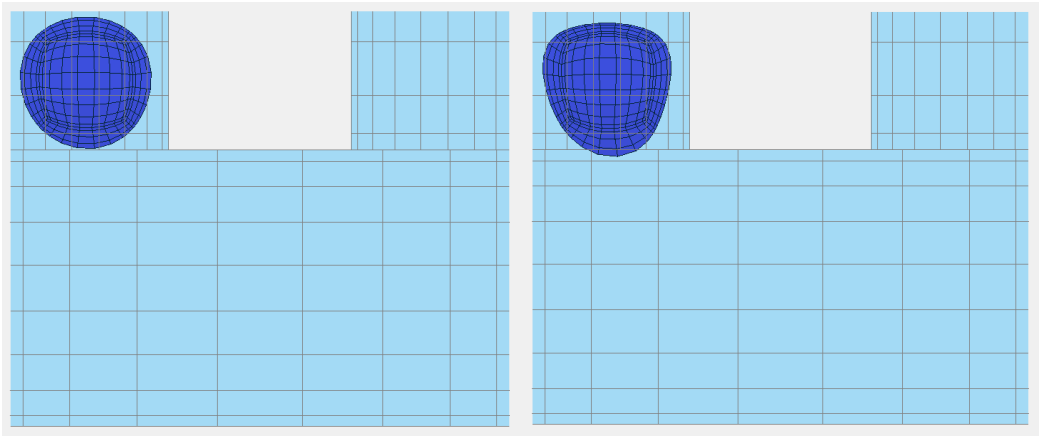

(a) (b)

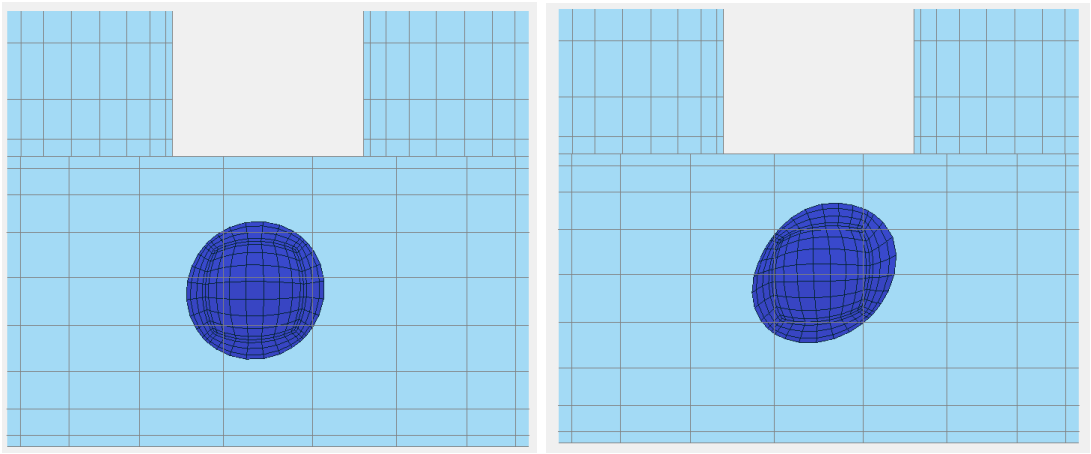

(c) (d)

Figure 24. Droplet deformation for Ca = 0.01 at t = 0.5 (a) Ca = 0.05 at t = 0.5 (b) Ca = 0.01 at t = 3 (c) Ca = 0.05 at t = 3 (d).

5.2. Influence of viscosity ratio

The effect of the viscosity ratio was studied for λ = 0.2, 0.5, 1. For this study, z_{c0} = 5, *Ca* = 0.03, *Bo* = 0, and *h* = 3.33.

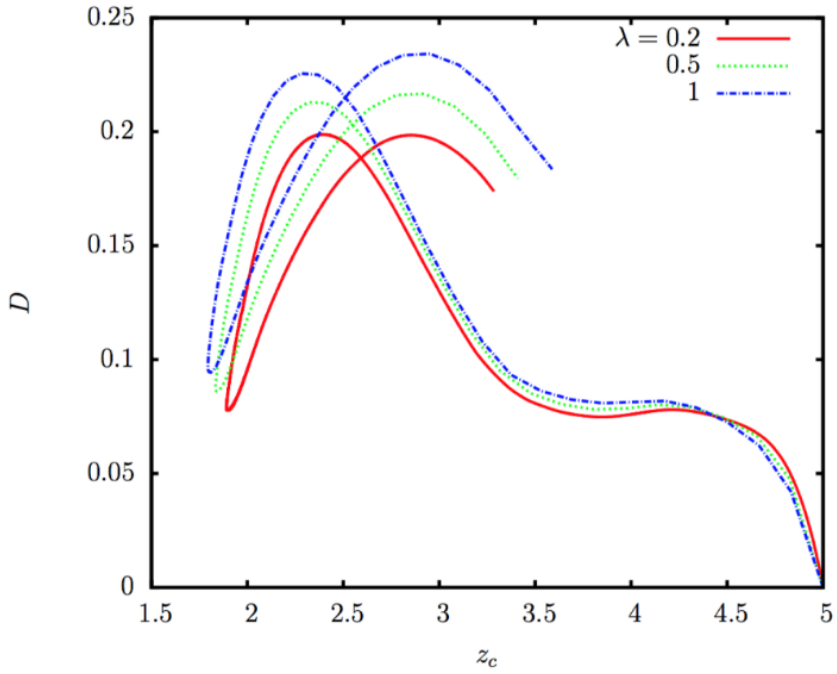

Figure 25. Droplet deformation D is plotted as a function of its centroid location z_c. Cases for λ = 0.2, 0.5, 1 are included.

All cases show the trend of having the largest deformation at the corners of the return bend and the smallest deformation at the inlet channel, middle of the return bend, and outlet channel. For Figure 25 the deformation increases with increasing viscosity ratio.

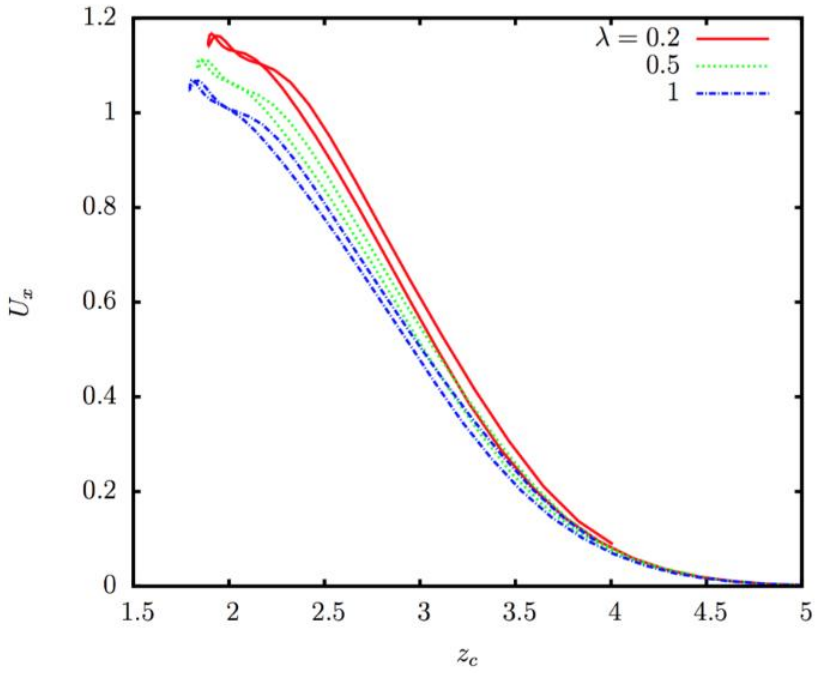

Figure 26. Droplet velocity U_x as a function of its centroid location z_c. Cases for λ=0.2, 0.5, 1 are included.

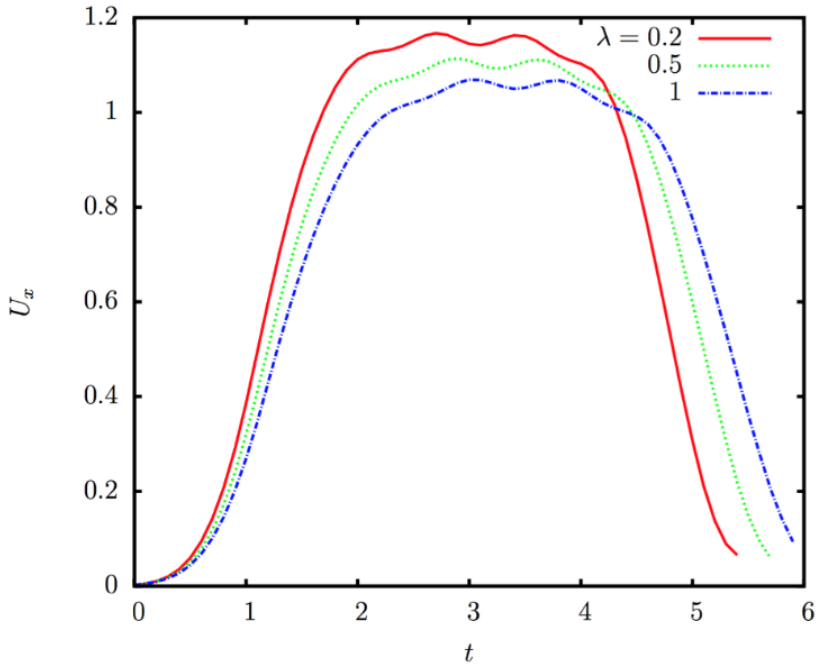

Figure 27. Droplet velocity U_x as a function of time. Cases for λ=0.2, 0.5, 1 are included.

Figure 26 and 27 show that the velocity U_x decreases with an increase in the viscosity ratio. This is because the droplet will experience greater resistance with an increase in viscous forces. The droplet centroid reaches the middle of the return bend in less time for lower viscosity ratios because of the increased velocity U_x.

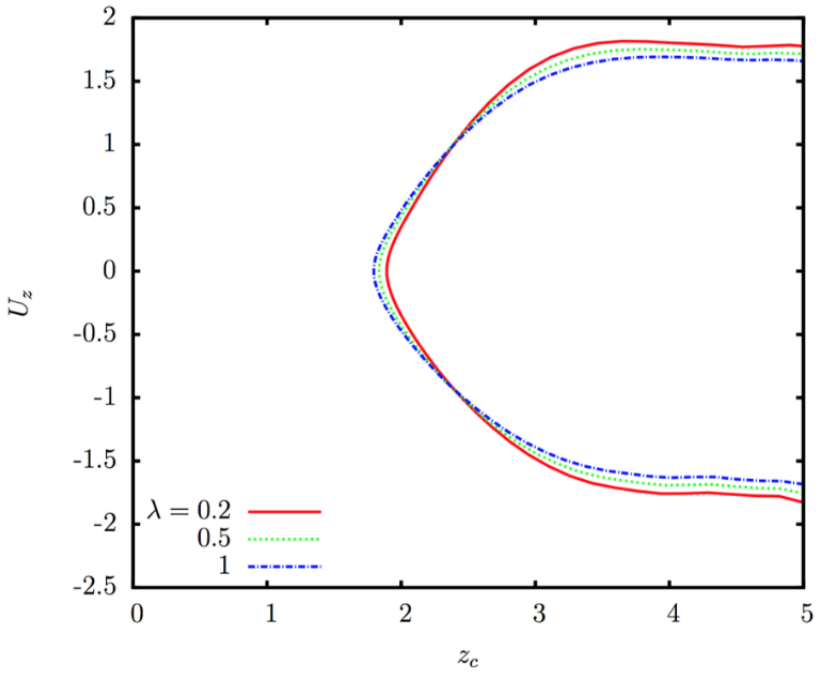

Figure 28. Droplet velocity U_z as a function of its centroid location z_c. Cases for λ=0.2, 0.5, 1 are included.

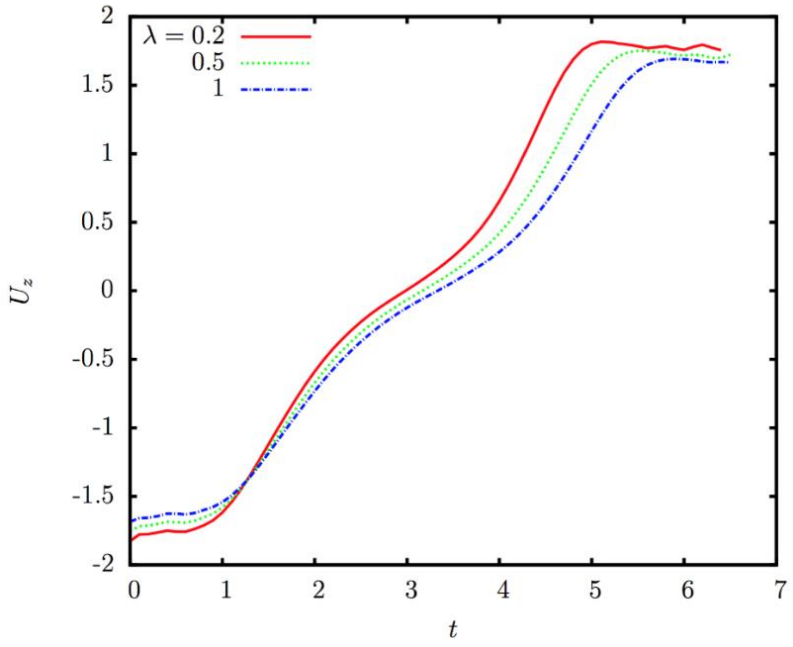

Figure 29. Droplet velocity U_z as a function of time. Cases for λ=0.2, 0.5, 1 are included.

In Figure 28 and 29 for a lower viscosity ratio, the droplet centroid moves with greater velocity, U_z, in the inlet and outlet channels, and the trajectory is higher in the return bend.

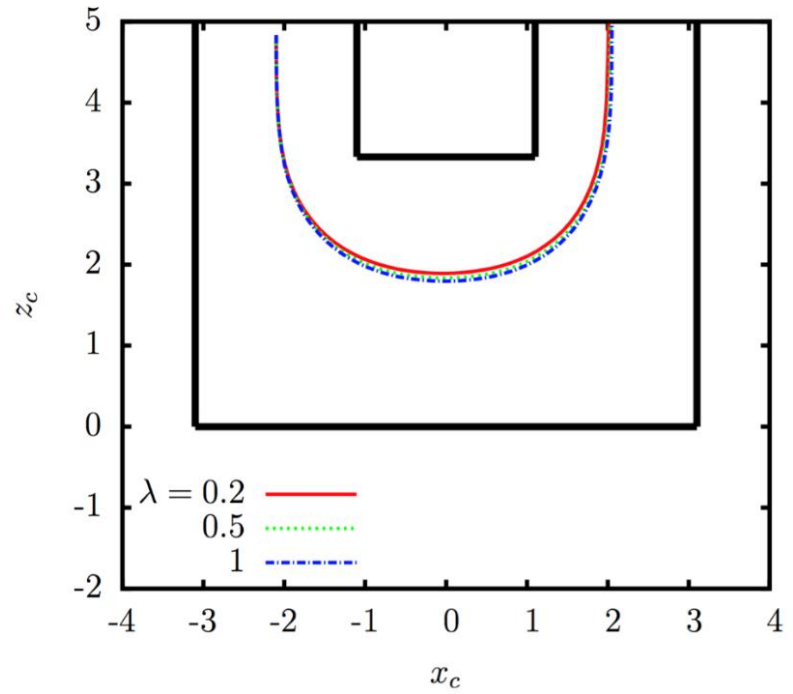

Figure 30. Trajectory of the droplet centroid. Cases for λ=0.2, 0.5, 1 are included.

Figure 30 shows that the droplet centroid migrates father down in the return bend when the viscosity ratio is higher.

For the cases considered, as the viscosity ratio increases from 0.2 to 1, the deformation increases, the velocity is reduced for both U_x and U_z, and the droplet migrates farther down in the return bend. Simulations were run for cases of cases λ=0.5, 1 and the same trends were recognized.

5.3. Influence of channel dimension h

The effect of changing the channel dimension h was studied. Cases of h = 2.5, 3, and 3.33 were considered. For this study, z_{c0} = 5, Ca = 0.03, Bo = 0, and $\lambda = 0.2$.

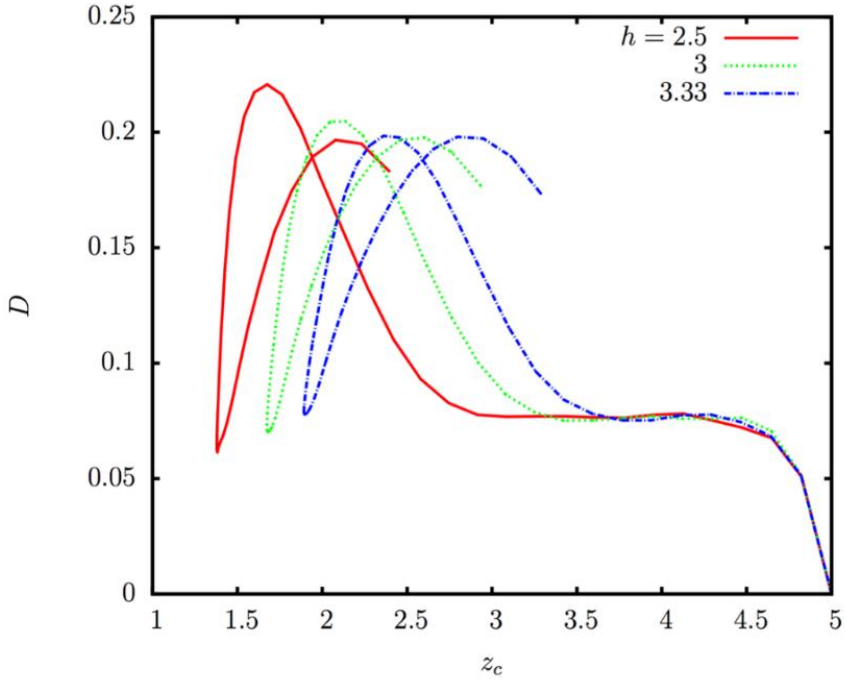

Figure 31. Droplet deformation D as a function of its centroid location z_c. Cases for h = 3.33, 3, and 2.5 are included.

For the cases of a smaller h value, Figure 31 shows increased deformation at the first corner of the bend and a slight decrease in deformation near the middle of the return bend.

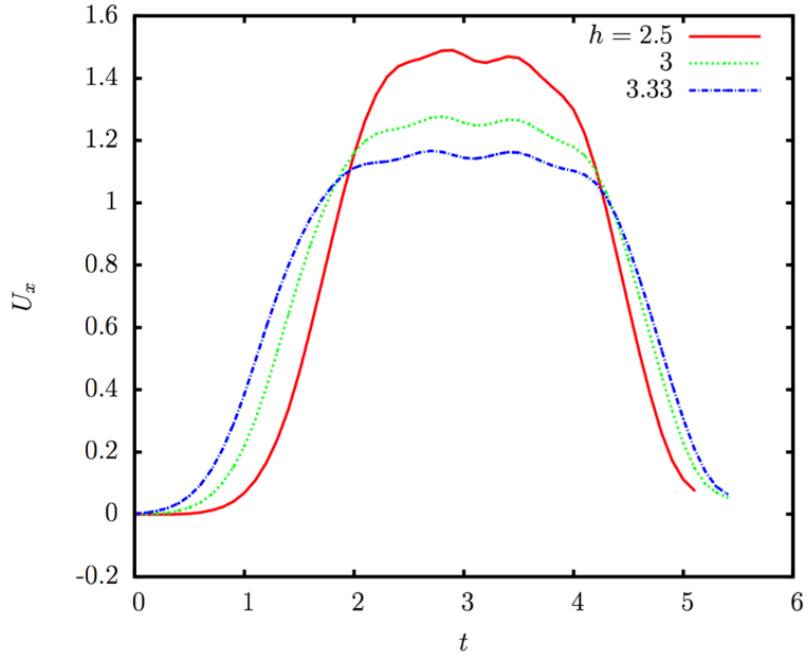

Figure 32. Droplet velocity U_x as a function of time. Cases for h = 3.33, 3, and 2.5 are included.

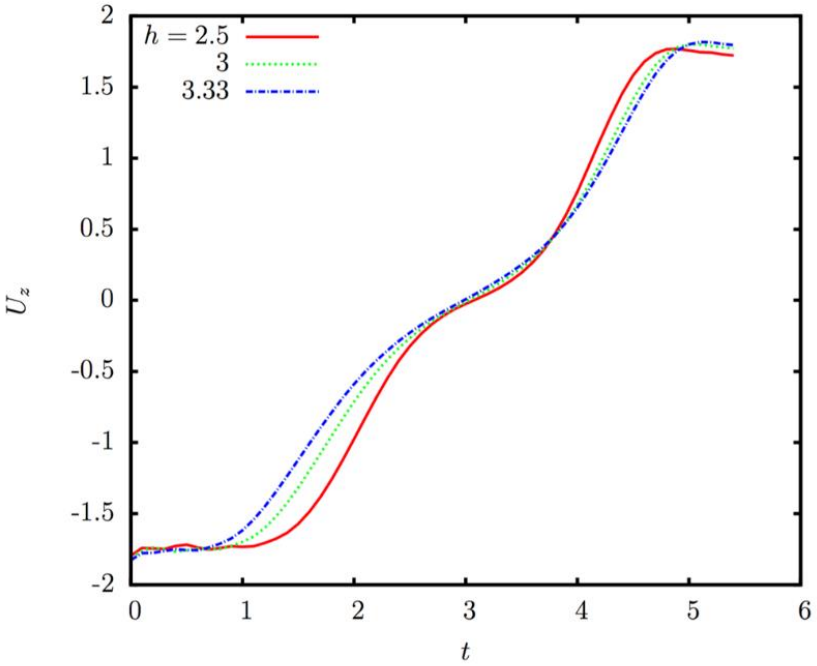

Figure 33. Droplet velocity U_z as a function of time. Cases for h = 3.33, 3, and 2.5 are included.

Figure 32 and 33 show that with a small h value, it takes longer for the droplet centroid to get into and out of the return bend, but the velocity U_z is greater than for large h values near the middle of the return bend.

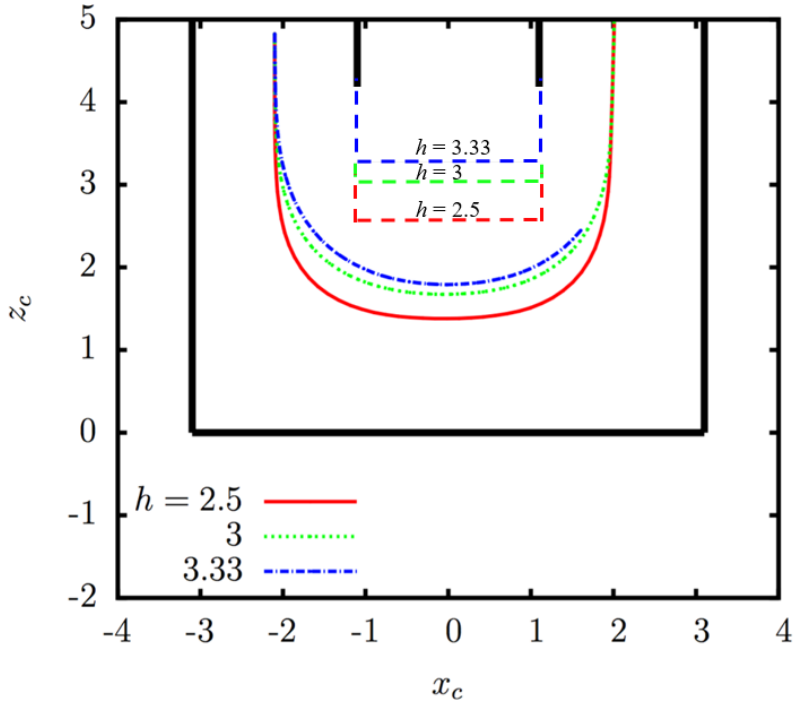

Figure 34. Trajectory of the droplet centroid. Cases for h = 3.33, 3, and 2.5 are inlcuded.

The varied return bend geometry compare to the droplet centroid trajectory is depicted in Figure 34. The droplet centroid migrates farther down in the return bend for smaller h values.

For these cases, as h is decreased, the droplet deformation increases, the droplet takes longer to travel into the return bend but the velocity, U_x and U_z, peaks at a higher value, and the droplet migrates significantly lower in the return bend. The cases of h = 1.5 and 2 were also considered, but the simulation failed to finish running due to the large amount of droplet deformation.

5.4. Influence of gravity

Because of the microscale dimensions of the microfluidic chip, gravity was not expected to affect the dynamics of the droplet. The previous statement was verified by calculating Bo = 8.34 x 10^{-4}. Since Bo << 1, the surface tension forces are dominant over the gravitational force. For a theoretical study where gravity has an effect, the cases of Bo = 0.5, 1, and 2 were considered. For this study, z_{c0} = 5, Ca = 0.03, $\lambda = 0.2$, and h = 3.33. The following figures show the deformation as a function of the centroid location z_c, the velocities U_x and U_z as a function of time, and the centroid trajectory.

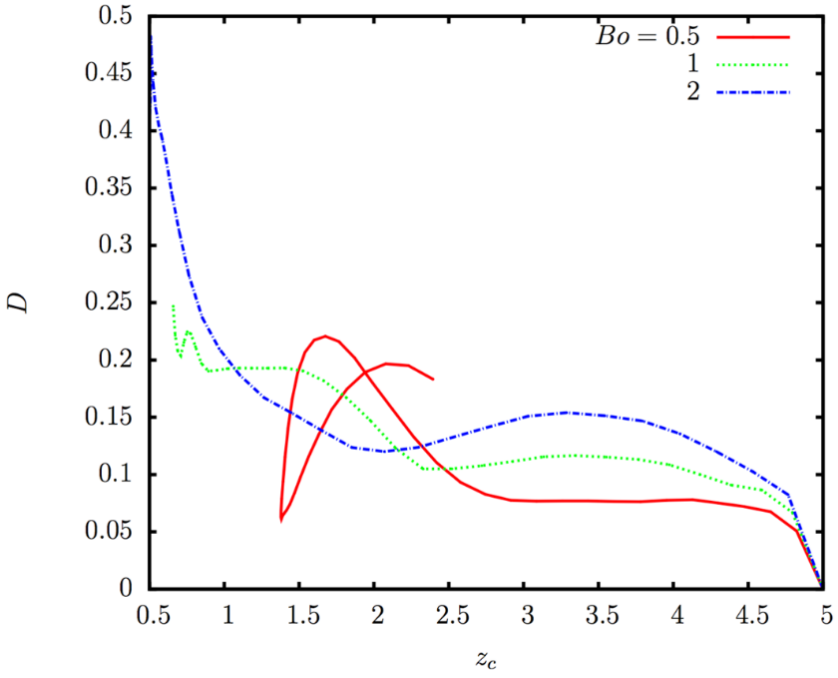

Figure 35. Droplet deformation D as a function of its centroid location z_c. Cases for Bo = 0.5, 1, and 2 are included.

In Figure 35 it is seen that the droplet deformation significantly increases with increasing Bo number.

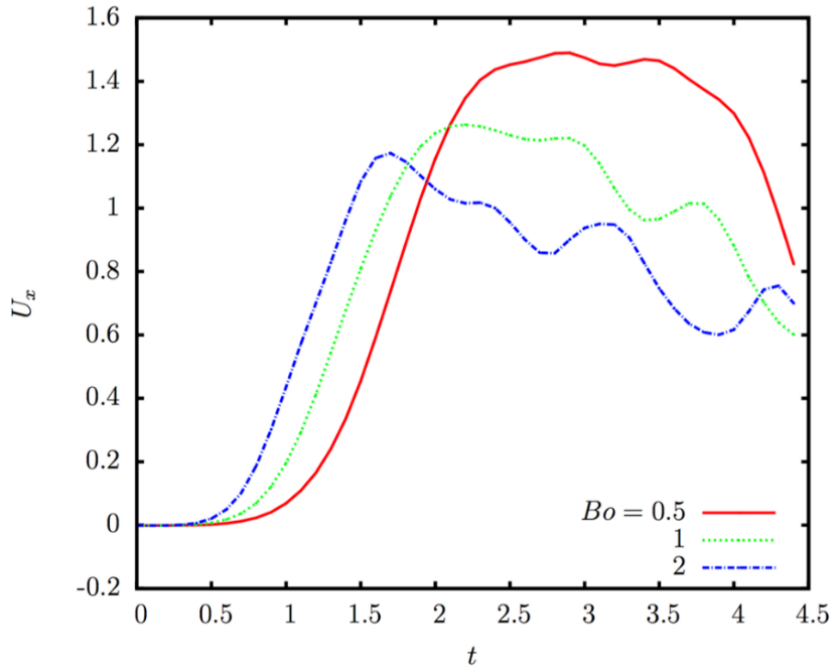

Figure 36. Droplet velocity U_x as a function of its centroid location z_c. Cases for Bo = 0.5, 1, and 2 are included.

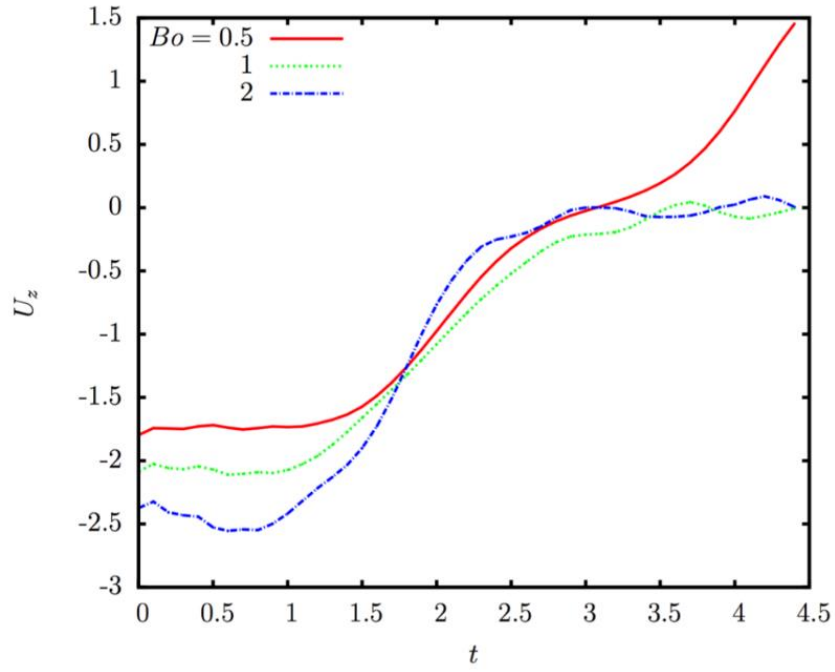

Figure 37. Droplet velocity U_z as a function of its centroid location z_c. Cases for Bo = 0.5, 1, and 2 are included.

In Figure 37 it is seen that with increasing Bo number the droplet velocity U_z increases in the inlet channel.

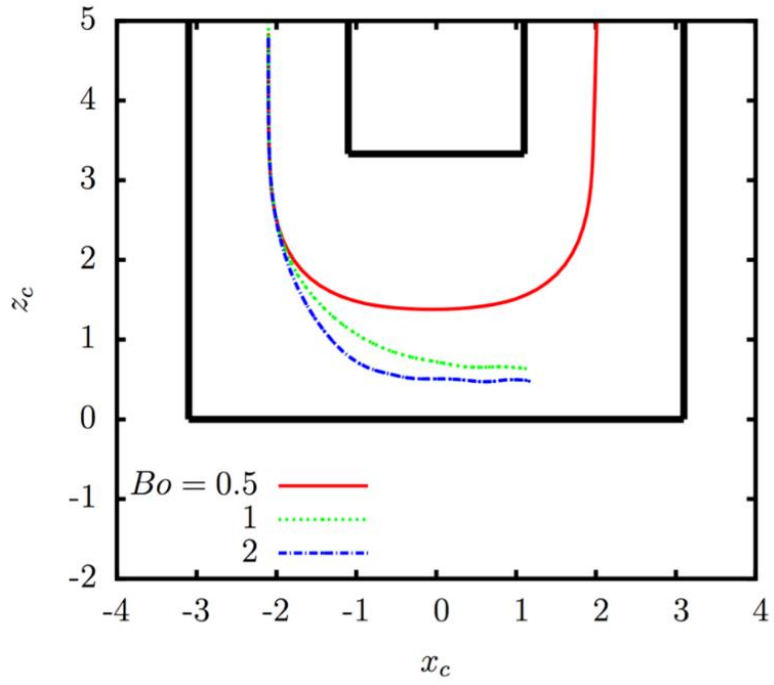

Figure 38. Trajectory of the droplet. Cases for Bo = 0.5, 1, and 2 are included.

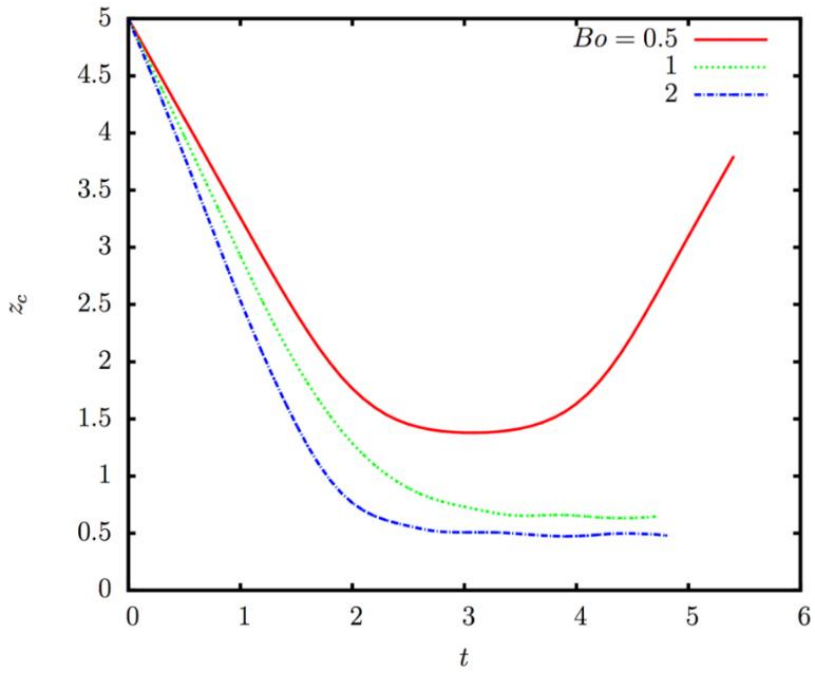

Figure 39. Droplet centroid location z_c. Cases for Bo = 0.5, 1, and 2 are included.

In Figure 38 and 39 the droplet centroid migrates significantly farther down in the return bend. The additional force in the z-direction causes the droplet to press into the bottom wall of the return bend.

For these cases, as the Bo number increased, the droplet deformation increased, the velocity U_x decreased, the velocity U_z increased, and the droplet centroid migrated toward the bottom of the return bend. From these results, it is recognized that an applied force can have a large effect on droplet migration. Future research could consider using a ferrofluid as the discontinuous phase and applying a magnetic field on the system. A summary of the droplet trends from the computational studies is provided by Table 2.

Table 2. Summary of droplet trends in microfluidic return bend.

	U_x	U_z	**Deformation**	**Depth of Migration**
Ca ↑	↑	↑	↑	↓
λ ↑	↓	↓	↑	↑
h ↑	↓	↑	↓	↓
Bo ↑	↓	↑	↓	↑

5.5. Limitations of the computational model

This model assumes incompressible, Newtonian fluids under Stokes flow conditions. The droplet contains fluid that is immiscible with the suspending fluid. It is recognized that in future experiments the fluid for the droplet will be media that contains cells. The model will be improved by increasing the number of spectral points, however, increasing the number of spectral points also increases the computational cost of the simulation. The relative errors for the velocity, U_z, and deformation were already low (Figure 13). This model assumed perfect

geometry with 90° bends which is difficult to achieve in manufacturing. Although this model has limitations, it is useful in guiding the design of microfluidic chips for future experiments.

6. CONCLUSION

This research shows a process for fabricating polymer cast microfluidic chips that allows for rapid prototyping with a reduced cost. Droplets were formed using a T-junction and their motion was analyzed in the first half of the return ben. Generated plots showed that the droplet deformation increased as the droplet moved from the inlet channel and entered into the return bend. The velocity U_z was greatest in the inlet channel and decreased as the droplet entered the return bend. The velocity U_x was smallest in the inlet channel and increased as the droplet entered the return bend.

When employing a 3D spectral boundary element method to study the influence that surface tension, viscosity, gravity, and channel dimensions have on droplet dynamics, the deformation, velocity, and trajectory of a droplet was characterized for several cases. The dynamics of droplet movement in this specific geometry was previously unknown. For the Ca number study, the trends showed that as the Ca number increased, the droplet deformation increased, the U_x and U_z velocities increased, and the trajectory of the droplet was higher as it moved through the return bend. For the viscosity ratio study, as the viscosity ratio increased from 0.2 to 1, the deformation increased, the velocity was reduced for both U_x and U_z, and the droplet migrated farther down in the return bend. As h was decreased in the channel depth study, the droplet deformation decreased, the droplet took longer to travel into the return bend, and the droplet migrated significantly lower in the return bend. For the study on the influence of gravity, it was determined that a gravitational force can have a large effect on droplet migration.

Returning to the goal of achieving cell deposition into 3D spheroid arrays, here are the recommendations for the future design of the microfluidic chip. If a 3D spheroid were connected to the bottom of a return bend, it would be necessary to have a droplet migrate toward the bottom

of the array for deposition. These results show that for a droplet to move toward the bottom of the return bend, the capillary number should be small, the viscosity ratio should be large, and the channel dimension h should be small. This microfluidic chip design would promote the droplet moving into the 3D spheroid that would be attached to the bottom of the channel.

REFERENCES

[1] C. Tomaro-Duchesneau, S. Saha, M. Malhotra, I. Kahouli, and S. Prakash, "Microencapsulation for the Therapeutic Delivery of Drugs, Live Mammalian and Bacterial Cells, and Other Biopharmaceutics: Current Status and Future Directions," *Journal of pharmaceutics*, vol. 2013, pp. 103527–103527, 2013.

[2] M. Neves *et al.*, "Exploring sialyl-Tn expression in microfluidic-isolated circulating tumour cells: A novel biomarker and an analytical tool for precision oncology applications," *New Biotechnology*, vol. 49, pp. 77–87, 2019.

[3] H. Cao, X. Zhou, and Y. Zeng, "Microfluidic exponential rolling circle amplification for sensitive microRNA detection directly from biological samples," *Sensors and Actuators, B: Chemical*, vol. 279, pp. 447–457, 2019.

[4] P. Zhang *et al.*, "Ultrasensitive detection of circulating exosomes with a 3D-nanopatterned microfluidic chip," *Nature Biomedical Engineering*, 2019.

[5] H. Chen, Z. Zhang, H. Liu, Z. Zhang, C. Lin, and B. Wang, "Hybrid magnetic and deformability based isolation of circulating tumor cells using microfluidics," *AIP Advances*, vol. 9, no. 2, 2019.

[6] C.-C. Yu *et al.*, "Random and aligned electrospun PLGA nanofibers embedded in microfluidic chips for cancer cell isolation and integration with air foam technology for cell release 02 Physical Sciences 0299 Other Physical Sciences 03 Chemical Sciences 0306 Physical Chemistry (incl. Structural)," *Journal of Nanobiotechnology*, vol. 17, no. 1, 2019.

[7] C. Chen, B. T. Mehl, S. A. Sell, and R. Scott Martin, "Use of electrospinning and dynamic air focusing to create three-dimensional cell culture scaffolds in microfluidic devices," *Analyst*, vol. 141, no. 18, pp. 5311–5320, 2016.

[8] T. W. Murphy, J. Sheng, L. B. Naler, X. Feng, and C. Lu, "On-chip manufacturing of synthetic proteins for point-of-care therapeutics," *Microsystems and Nanoengineering*, vol. 5, no. 1, 2019.

[9] J. Zhou, A. Kulasinghe, A. Bogseth, K. O'Byrne, C. Punyadeera, and I. Papautsky, "Isolation of circulating tumor cells in non-small-cell-lung-cancer patients using a multi-flow microfluidic channel," *Microsystems and Nanoengineering*, vol. 5, no. 1, 2019.

[10] S. H. Lee and B.-H. Jun, "Advances in dynamic microphysiological organ-on-a-chip: Design principle and its biomedical application," *Journal of Industrial and Engineering Chemistry*, vol. 71, pp. 65–77, 2019.

[11] M. Hamidović, W. Haselmayr, A. Grimmer, R. Wille, and A. Springer, "Passive droplet control in microfluidic networks: A survey and new perspectives on their practical realization," *Nano Communication Networks*, vol. 19, pp. 33–46, 2019.

[12] J. Lian, X. Luo, X. Huang, Y. Wang, Z. Xu, and X. Ruan, "Investigation of microfluidic co-flow effects on step emulsification: Interfacial tension and flow velocities," *Colloids and Surfaces A: Physicochemical and Engineering Aspects*, vol. 568, pp. 381–390, 2019.

[13] K. Ren, J. Zhou, and H. Wu, "Materials for Microfluidic Chip Fabrication," *Acc. Chem. Res.*, vol. 46, no. 11, pp. 2396–2406, Nov. 2013.

[14] C. Iliescu, H. Taylor, M. Avram, J. Miao, and S. Franssila, "A practical guide for the fabrication of microfluidic devices using glass and silicon," *Biomicrofluidics*, vol. 6, no. 1, pp. 16505–1650516, Mar. 2012.

[15] M. Leester-Schädel, T. Lorenz, F. Jürgens, and C. Richter, "Fabrication of Microfluidic Devices," 2016, pp. 23–57.

[16] B. Gale *et al.*, *A Review of Current Methods in Microfluidic Device Fabrication and Future Commercialization Prospects*, vol. 3. 2018.
[17] V. Silverio and S. Cardoso, "Microfabrication Techniques for Microfluidic devices," 2018, pp. 25–51.
[18] M. Villegas, Z. Cetinic, A. Shakeri, and T. F. Didar, "Fabricating smooth PDMS microfluidic channels from low-resolution 3D printed molds using an omniphobic lubricant-infused coating," *Analytica Chimica Acta*, vol. 1000, pp. 248–255, 2018.
[19] M. Sun, Y. Xie, J. Zhu, J. Li, and J. C. T. Eijkel, "Improving the Resolution of 3D-Printed Molds for Microfluidics by Iterative Casting-Shrinkage Cycles," *Analytical Chemistry*, vol. 89, no. 4, pp. 2227–2231, 2017.
[20] C.-S. Yih, *Fluid Mechanics*. Michigan: West Rivers Press, 1979.
[21] G. P. Muldowney and J. J. L. Higdon, "A spectral boundary element approach to three-dimensional Stokes flow," *Journal of Fluid Mechanics*, vol. 298, pp. 167–192, 1995.
[22] P. Dimitrakopoulos and J. J. L. Higdon, "On the displacement of three-dimensional fluid droplets from solid surfaces in low-Reynolds-number shear flows," *Journal of Fluid Mechanics*, vol. 377, pp. 189–222, 1998.
[23] Y. Wang and P. Dimitrakopoulos, "A three-dimensional spectral boundary element algorithm for interfacial dynamics in Stokes flow," *Physics of Fluids*, vol. 18, no. 8, 2006.
[24] C. Pozrikidis, *Boundary integral and singularity methods for linearized viscous flow*. Cambridge University Press, 1992.
[25] B. T. Kelly, J.-C. Baret, V. Taly, and A. D. Griffiths, "Miniaturizing chemistry and biology in microdroplets," *Chemical Communications*, no. 18, pp. 1773–1788, 2007.
[26] Y. Wang, "Numerical Studies of Stokes Flow in Confined Geometries," Master of Science, University of Maryland, College Park, 2004.